



UNIVERSITY OF LEEDS

This is a repository copy of *Thermodynamic modelling of alkali-activated slag cements*.

White Rose Research Online URL for this paper:
<http://eprints.whiterose.ac.uk/136456/>

Version: Accepted Version

Article:

Myers, RJ, Lothenbach, B, Bernal, SA et al. (1 more author) (2015) Thermodynamic modelling of alkali-activated slag cements. *Applied Geochemistry*, 61. pp. 233-247. ISSN 0883-2927

<https://doi.org/10.1016/j.apgeochem.2015.06.006>

© 2015 Elsevier Ltd. This manuscript version is made available under the CC-BY-NC-ND 4.0 license <http://creativecommons.org/licenses/by-nc-nd/4.0/>.

Reuse

This article is distributed under the terms of the Creative Commons Attribution-NonCommercial-NoDerivs (CC BY-NC-ND) licence. This licence only allows you to download this work and share it with others as long as you credit the authors, but you can't change the article in any way or use it commercially. More information and the full terms of the licence here: <https://creativecommons.org/licenses/>

Takedown

If you consider content in White Rose Research Online to be in breach of UK law, please notify us by emailing eprints@whiterose.ac.uk including the URL of the record and the reason for the withdrawal request.

1 **Thermodynamic modelling of alkali-activated slag**
2 **cements**
3

4 **Rupert J. Myers¹, Barbara Lothenbach², Susan A. Bernal¹,**

5 **John L. Provis^{1*}**

6
7 ¹ Department of Materials Science and Engineering, The University of Sheffield, Sir Robert
8 Hadfield Building, Mappin St, Sheffield S1 3JD, UK

9
10 ² Laboratory for Concrete and Construction Chemistry, EMPA, Dübendorf, 8600,
11 Switzerland

12
13 * To whom correspondence should be addressed. Email j.provis@sheffield.ac.uk, phone +44
14 114 222 5490, fax +44 114 222 5493

15
16 **Keywords**

17
18 Thermodynamic modelling; alkali-activated slag cement; C-A-S-H; phase diagram; layered double
19 hydroxide; zeolite

20
21 **Abstract**

22
23 This paper presents a thermodynamic modelling analysis of alkali-activated slag-based cements,
24 which are high performance and potentially low-CO₂ binders relative to Portland cement. The

25 thermodynamic database used here contains a calcium (alkali) aluminosilicate hydrate ideal solid
26 solution model (CNASH_ss), alkali carbonate and zeolite phases, and an ideal solid solution model
27 for a hydrotalcite-like Mg-Al layered double hydroxide phase. Simulated phase diagrams for NaOH-
28 and Na₂SiO₃-activated slag-based cements demonstrate the high stability of zeolites and other solid
29 phases in these materials. Thermodynamic modelling provides a good description of the chemical
30 compositions and types of phases formed in Na₂SiO₃-activated slag cements over the most relevant
31 bulk chemical composition range for these cements, and the simulated volumetric properties of the
32 cement paste are consistent with previously measured and estimated values. Experimentally
33 determined and simulated solid phase assemblages for Na₂CO₃-activated slag cements were also
34 found to be in good agreement. These results can be used to design the chemistry of alkali-activated
35 slag-based cements, to further promote the uptake of this technology and valorisation of metallurgical
36 slags.

37

38

39 **1. Introduction**

40

41 Development of high performance and low CO₂ cement-based materials is needed to reduce the CO₂
42 footprint of the construction industry. Alkali-activated cements are formed through the reaction of a
43 soluble alkali source (the ‘activator’), water and aluminosilicate precursors, which are often sourced
44 as industrial by-products (Provis, 2014). Blast furnace slag is one such material, and forms an
45 important component of many modern cements, including use as the main raw material in production
46 of alkali-activated slag (AAS) cements (Provis and Bernal, 2014). The reactive component of blast
47 furnace slag is a calcium-magnesium aluminosilicate glass that dissolves under the high pH conditions
48 provided by the activator to form a hydrated phase assemblage that consolidates into a hardened
49 binder. AAS-based cements are attractive solutions for waste valorisation and utilisation of industrial
50 by-products, e.g. in immobilisation matrices for radioactive wastes (Bai et al., 2011), and can provide
51 substantial CO₂ savings relative to Portland cement (PC)-based materials (McLellan et al., 2011).

52 Understanding the durability of alkali-activated cements is a key scientific challenge facing their
53 commercial uptake and utilisation (van Deventer et al., 2012). Durability is intimately linked to the
54 chemistry and microstructure of these cements, and thus depends on physicochemical factors
55 including chemical shrinkage and the solid phase assemblage formed.

56

57 The main component of hardened AAS-based materials is a calcium (alkali) aluminosilicate hydrate
58 ($C\text{-}(N\text{-})A\text{-}S\text{-}H$) gel¹ that is poorer in Ca (molar Ca/Si ratio ≈ 1 (Shi et al., 2006)) and richer in Al
59 (molar Al/Si ratio > 0.1 (Le Saoût et al., 2011; Myers et al., 2013; Richardson et al., 1994)) than the
60 calcium (alumino)silicate hydrate ($C\text{-}(A\text{-})S\text{-}H$) gel formed in hydrated PC (Taylor et al., 2010). The
61 solid phase assemblage in AAS cements contains phases other than $C\text{-}(N\text{-})A\text{-}S\text{-}H$ gel, typically
62 including Mg-Al layered double hydroxide (LDH) phases (Richardson et al., 1994; Wang and
63 Scrivener, 1995) and aluminoferrite-mono (AFm) type phases including strätlingite (C_2ASH_8) (Ben
64 Haha et al., 2012; Richardson et al., 1994; Wang and Scrivener, 1995), and calcium
65 monocarboaluminate hydrate (C_4AcH_{11}) in Na_2CO_3 (N_c)-activated slag (N_c -AS) cement (Shi et al.,
66 2006). Katoite (C_3AH_6) (Bonk et al., 2003), zeolites including gismondine and heulandite (Bernal et
67 al., 2015; Bernal et al., 2011), and the third aluminate hydrate (TAH) (Myers et al., 2015a), which is
68 described as a poorly ordered $Al(OH)_3$ phase (Taylor et al., 2010), may additionally form in AAS
69 cements. Recently, evidence for the formation of alkali aluminosilicate (hydrate) ($N\text{-}A\text{-}S\text{(-}H)$) gels in
70 AAS cement has been presented (Myers et al., 2015a; Myers et al., 2013); this phase is considered to
71 be similar to the ‘geopolymer’ gels formed through alkali-activation of low-Ca raw materials (Provis
72 et al., 2005).

73

74 Thermodynamic modelling can be used to predict the chemistry of hydrated/alkali-activated cements,
75 assuming equilibrium between the solid reaction products and pore solution (Atkins et al., 1992;
76 Lothenbach, 2010; Savage et al., 2011), which is critically important in understanding their long-term
77 behaviour, e.g. in radioactive waste disposal applications (Glasser and Atkins, 1994). This approach

¹ The various alkalis that may be incorporated into $C\text{-}(N\text{-})A\text{-}S\text{-}H$ gel are all represented by Na here because the alkali source in an alkali-activated cement is typically Na-based. Cement chemistry notation is used throughout the text: C = CaO; S = SiO₂; A = Al₂O₃; N = Na₂O; H = H₂O; M = MgO; c = CO₂; and s = SO₃.

78 has been applied to AAS cements in the past (Lothenbach and Gruskovnjak, 2007), however the
79 calcium silicate hydrate (C-S-H) thermodynamic model (Kulik and Kersten, 2001) used in that study
80 does not explicitly define the uptake of Al and Na which is needed to fully describe C-(N)-A-S-H gel.
81 Chemically complete definitions of Al chemistry in the thermodynamic models used to simulate the
82 phases formed in AAS-based cements are important in enabling accurate prediction of the chemistry
83 of these cements. The inclusion of alkalis as a key component in thermodynamic models for C-(N)-A-
84 S-H gel is also important to enable correct description of the solubility relationships of this phase
85 under the high pH conditions (>12) and alkali concentrations (tens to hundreds of mmol/L) relevant to
86 the majority of cementitious materials (Myers et al., 2014).

87

88 The CNASH_ss thermodynamic model used in the current paper was recently developed (Myers et
89 al., 2014) to formally account for Na and tetrahedral Al incorporated in Ca/Si < 1.3 C-(N)-A-S-H gel.
90 Here, this thermodynamic model is used to simulate the chemistry of AAS cements activated by
91 aqueous solutions of NaOH ((NH)_{0.5}), Na₂SiO₃ (NS), Na₂Si₂O₅ (NS₂) and Nc. This thermodynamic
92 model can describe a large set of solubility data for the CaO-(Na₂O,Al₂O₃)-SiO₂-H₂O and AAS
93 cement systems, and closely matches the published chemical compositions of calcium aluminosilicate
94 hydrate (C-A-S-H) gel, and the volumetric properties of C-(N)-A-S-H gel measured in a sodium
95 silicate-activated slag cement (Myers et al., 2014). The CNASH_ss thermodynamic model is assessed
96 here in terms of the prediction of solid phase assemblages and the Al content of C-(N)-A-S-H gel over
97 the bulk slag chemical composition range which is most relevant to AAS cement-based materials.
98 These simulations are performed using the Gibbs energy minimisation software GEM-Selektor v.3
99 (<http://gems.web.psi.ch/>) (Kulik et al., 2013; Wagner et al., 2012) and an expanded thermodynamic
100 database for cements, based on the CEMDATA07 database (Babushkin et al., 1985; Hummel et al.,
101 2002; Lothenbach et al., 2008; Lothenbach and Winnefeld, 2006; Matschei et al., 2007; Möschner et
102 al., 2008; Möschner et al., 2009; Schmidt et al., 2008; Thoenen and Kulik, 2003) with the addition of
103 an updated definition of Mg-Al LDH intercalated with OH⁻ (MA-OH-LDH), and including some
104 zeolites and alkali carbonates. The results are discussed in terms of implications for the design of high
105 performance AAS-based cements.

106

107 **2. Methods**

108 **2.1 Thermodynamic model for C-(N-)A-S-H gel**

109 The CNASH_ss thermodynamic model (Myers et al., 2014) is formulated as an ideal solid solution
110 with mixing on six of eight sublattice sites to give three C-S-H gel end-members, one calcium (alkali)
111 silicate hydrate (C-(N-)S-H) gel end-member, two C-A-S-H gel end-members and two C-(N-)A-S-H
112 gel end-members (Table 1). End-member chemical compositions are defined in this model by
113 extension of the ‘Substituted General Model’ (Richardson and Groves, 1993) for consistency with
114 tobermorite-like nanostructures containing no ‘interstratified Ca(OH)₂’ (Richardson, 2004), which
115 limits the applicability of the CNASH_ss thermodynamic model to Ca/Si ratios <1.3 in the C-(N-)A-
116 S-H gel. Pentahedral Al (Al[5]) and octahedral Al (Al[6]) are not explicitly considered in the end-
117 member structures described by CNASH_ss.

118

119 C-(N-)A-S-H gel is formally described in terms of non-cross-linked chain structures in the
120 CNASH_ss thermodynamic model, but without precluding representation of cross-linked tobermorite-
121 like chain structures, because these structural types cannot be differentiated by bulk chemical
122 composition alone. Thermodynamic calculations using the CNASH_ss thermodynamic model are
123 therefore also consistent with cross-linked C-(N-)A-S-H gel structural models such as those described
124 by the ‘Cross-linked Substituted Tobermorite Model’ (CSTM) (Myers et al., 2013). Full details of the
125 development and implementation of the CNASH_ss thermodynamic model are given in (Myers et al.,
126 2014).

127

128 **2.2 Thermodynamic model for MA-OH-LDH**

129 Thermodynamic data for MA-OH-LDH were reformulated into an ideal solid solution thermodynamic
130 model (MA-OH-LDH_ss) containing three end-members with Mg/Al ratios of 2, 3 and 4 (Table 1) to

131 match the known chemical composition range of this solid solution ($Mg_{(1-x)}Al_x(OH)_{(2+x)} \cdot mH_2O$, $0.2 \leq x$
132 ≤ 0.33 (Richardson, 2013)).

133

134 Recalculation of recently published solubility data for $Mg/Al = 2$ MA-OH-LDH (M_4AH_{10}) (Gao and
135 Li, 2012) and existing solubility data for this phase (Bennett et al., 1992) was performed in GEM-
136 Selektor v.3 (<http://gems.web.psi.ch/>) (Kulik et al., 2013; Wagner et al., 2012) using the dissolution
137 reaction eq.(1):

138



140

141 where K_s is the solubility product. Solubility data for this phase were also calculated using the
142 additivity method (Anderson and Crerar, 1993) with brucite ($Mg(OH)_2(s)$), magnesite ($MgCO_3(s)$)
143 (Table 1), and hydrotalcite ($Mg_{0.74}Al_{0.26}(OH)_2(CO_3)_{0.13} \cdot 0.39H_2O(s)$) (Allada et al., 2005) constituents.

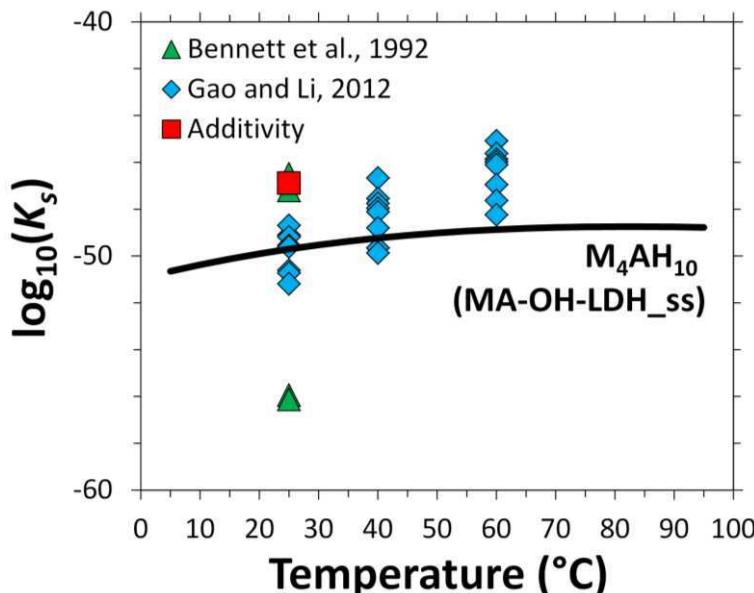
144

145 The recalculation results indicate that the solubility product used previously by Lothenbach and
146 Winnefeld (2006) to describe this phase ($\log_{10}(K_s) = -56.02$ at $25^\circ C$ and 1 bar), taken from the low
147 solubility data reported by Bennett et al. (1992), is not consistent with the solubility data reported by
148 Gao and Li (Gao and Li, 2012) (Figure 1). Here, a solubility product of $\log_{10}(K_s) = -49.70$ at $25^\circ C$ and
149 1 bar is selected for improved consistency with the solubility data reported by Gao and Li (Gao and
150 Li, 2012). The standard heat capacity and entropy of this phase are adapted from the thermodynamic
151 data reported by Allada et al. (Allada et al., 2005) for $Mg_{0.74}Al_{0.26}(OH)_2(CO_3)_{0.13} \cdot 0.39H_2O$ using the
152 additivity method with $Mg(OH)_2(s)$ and $MgCO_3(s)$ constituents, i.e. the standard heat capacity for
153 M_4AH_{10} is calculated via eq.(2):

154

155 $Cp^o_{M_4AH_{10}} = 2 \left(\frac{1}{0.26} Cp^o_{Mg_{0.74}Al_{0.26}(OH)_2(CO_3)_{0.13} \cdot 0.39H_2O} - 0.5Cp^o_{MgCO_3} - 0.346Cp^o_{Mg(OH)_2} \right)$ (2)

156



157
 158 Figure 1. Comparison between the recalculated solubility data (Bennett et al., 1992; Gao and Li,
 159 2012), results using the additivity method, and calculated solubility of the M_4AH_{10} end-member of the
 160 MA-OH-LDH_ss thermodynamic model used in this work (thick black line) ($P = 1$ bar). The green
 161 triangles at $\log_{10}(K_s) = -56.02$ ($25^\circ C$ and 1 bar), represents the solubility product used previously to
 162 describe this phase in the cement chemistry literature.
 163

164 Standard entropies and heat capacities for Mg/Al = 3 MA-OH-LDH (M_6AH_{12}) and Mg/Al = 4 MA-
 165 OH-LDH (M_8AH_{14}) were determined in the same manner (using solid constituents and a reaction
 166 analogous to eq.(2)), using the thermodynamic data reported by Allada et al. (Allada et al., 2005). A
 167 difference of -22.32 \log_{10} units was specified between the solubility products of M_4AH_{10} ($\log_{10}(K_s) = -$
 168 49.70) and M_6AH_{12} ($\log_{10}(K_s) = -72.02$), and between those of M_6AH_{12} and M_8AH_{14} ($\log_{10}(K_s) = -$
 169 94.34) at $25^\circ C$ and 1 bar, which is the difference between the solubility products of these phases when
 170 determined using the additivity method described here. A similar difference is found between reported
 171 thermodynamic data for MA-c-LDH ($Mg_4Al_2(OH)_{12}(CO_3) \cdot 4H_2O$, $\log_{10}(K_s) = -44.19$ (Rozov et al.,
 172 2011) and $Mg_6Al_2(OH)_{16}(CO_3) \cdot 5H_2O$, $\log_{10}(K_s) = -66.58$ (Rozov, 2010)), which suggests that the
 173 additivity approach is appropriate for these structurally-similar Mg-Al LDH phases. The three MA-
 174 OH-LDH phases M_4AH_{10} , M_6AH_{12} and M_8AH_{14} were specified as end-members of the ideal solid
 175 solution ‘MA-OH-LDH_ss’. This is justified because it has been shown that the assumption of
 176 mechanical (ideal) mixing is appropriate for modelling the total solubility of the structurally-similar
 177 hydrotalcite-pyroaurite solid solution series (Rozov et al., 2011). This MA-OH-LDH solid solution
 178 model is used in the thermodynamic modelling performed in this work.

179

180 **2.3 Occurrence of Mg, Fe and S-bearing phases**

181 Thermodynamic modelling of AAS cements requires consideration of additional constituent elements
182 outside the CaO-Na₂O-Al₂O₃-SiO₂-H₂O system, most notably Mg, Fe and S, as well as carbonates.
183 While the precipitation of Mg in AAS cement is generally well explained by its incorporation into
184 Mg-Al LDH phases (Ben Haha et al., 2011b; Richardson et al., 1994; Wang and Scrivener, 1995),
185 there is less consensus regarding the precipitation of Fe and S. Fe was excluded from this work,
186 consistent with the passivated state of this element in GBFS (Bernal et al., 2014a), and S released by
187 the slag was represented as S²⁻ with its oxidation limited by using a simulated N₂(g) atmosphere in the
188 thermodynamic modelling calculations.

189

190 **2.4 Other solid phases**

191 Thermodynamic data for cement-related solid phases other than C-(N)-A-S-H gel and MA-OH-LDH
192 were taken from the PSI/Nagra 12/07 thermodynamic database (Thoenen et al., 2013) and the
193 CEMDATA07 thermodynamic database, which was updated to include recently published data for
194 Al(OH)₃ and hydrogarnet phases (Dilnesa et al., 2014; Lothenbach et al., 2012) (Table 1).

195

196

Table 1. Thermodynamic properties of solid phases at 298.15 K and 1 bar.

Phases ^a	V° (cm ³ mol ⁻¹)	ΔH _f ° (kJ mol ⁻¹)	ΔG _f ° (kJ mol ⁻¹)	S° (J mol ⁻¹ K ⁻¹)	Cp° (J mol ⁻¹ K ⁻¹)	Reference
½AH ₃ (microcrystalline)	32.0	-1265	-1148	140	93.1	(Lothenbach et al., 2012)
Portlandite, CH	33.1	-985	-897	83.4	87.5	(Robie and Hemingway, 1995)
SiO ₂ (amorphous)	29.0	-903	-849	41.3	44.5	(Helgeson et al., 1978; Kulik and Kersten, 2001)
C ₂ AH ₈	90.1	-5278	-4696	450	521	(Lothenbach et al., 2012)
Katoite, (C ₃ AH ₆)	150	-5537	-5008	422	446	(Lothenbach et al., 2012)
C ₄ AH ₁₉	382	-1002	-8750	1120	1382	(Lothenbach et al., 2012)
CAH ₁₀	194	-5288	-4623	610	668	(Lothenbach et al., 2012)
Strätlingite, C ₂ ASH ₈	216	-6360	-5705	546	603	(Matschei et al., 2007)
Calcium monocarboaluminate hydrate, C ₄ AcH ₁₁	262	-8250	-7337	657	881	(Matschei et al., 2007)
Calcium hemicarboaluminate hydrate, C ₄ Ac _{0.5} H ₁₂	285	-8270	-7336	713	906	(Matschei et al., 2007)
Calcium tricarboaluminate hydrate, C ₆ Ac ₃ H ₃₂	650	-16792	-14566	1858	2121	(Matschei et al., 2007)
Ettringite, C ₆ As ₃ H ₃₂	707	-17535	-15206	1900	2174	(Lothenbach et al., 2008)
Gypsum, CsH ₂	74.7	-2023	-1798	194	186	(Hummel et al., 2002; Thoenen et al., 2013)
Anhydrite, Cs	45.9	-1435	-1322	107	99.6	(Hummel et al., 2002; Thoenen et al., 2013)
Lime, C	16.8	-635	-604	39.7	42.8	(Helgeson et al., 1978)
Brucite, MH	24.6	-923	-832	63.1	77.3	(Helgeson et al., 1978; Hummel et al., 2002; Thoenen et al., 2013)
MA-c-LDH, M ₄ AcH ₉	220	-7374	-6580	551	647	(Lothenbach et al., 2008)
C-(N-)A-S-H gel ideal solid solution end-members, 'CNASH_ss' (Myers et al., 2014)						
5CA, C _{1.25} A _{0.125} S ₁ H _{1.625}	57.3	-2491	-2293	163	177	(Myers et al., 2014)
INFCA, C ₁ A _{0.15625} S _{1.1875} H _{1.65625}	59.3	-2551	-2343	154	181	(Myers et al., 2014)
5CNA, C _{1.25} N _{0.25} A _{0.125} S ₁ H _{1.375}	64.5	-2569	-2382	195	176	(Myers et al., 2014)
INFCNA, C ₁ N _{0.34375} A _{0.15625} S _{1.1875} H _{1.3125}	69.3	-2667	-2474	198	180	(Myers et al., 2014)
INFCN, C ₁ N _{0.3125} S _{1.5} H _{1.1875}	71.1	-2642	-2452	186	184	(Myers et al., 2014)
T2C*, C _{1.5} S ₁ H _{2.5} ^b	80.6	-2721	-2465	167	237	(Myers et al., 2014)
T5C*, C _{1.25} S _{1.25} H _{2.5} ^b	79.3	-2780	-2517	160	234	(Myers et al.,

						2014) (Myers et al., 2014)
TobH*, $\text{C}_1\text{S}_{1.5}\text{H}_{2.5}$ ^b	85.0	-2831	-2560	153	231	
Calcium monosulfoaluminate-hydroxoaluminate hydrate non-ideal solid solution (Matschei et al., 2007)						
Calcium monosulfoaluminate hydrate, $\text{C}_4\text{AsH}_{12}$	309	-8750	-7779	821	942	(Matschei et al., 2007)
C_4AH_{13}	274	-8300	-7324	700	930	(Lothenbach et al., 2012)
MA-OH-LDH ideal solid solution end-members, ‘MA-OH-LDH_ss’						
M_4AH_{10}	219	-7160	-6358	549	648	(Allada et al., 2005; Richardson, 2013)
M_6AH_{12}	305	-9007	-8023	675	803	This study ^c
M_8AH_{14}	392	-10853	-9687	801	958	This study ^c
Carbonates						
Aragonite, $\text{C}_{\underline{\text{C}}}$	34.2	-1207	-1128	90.2	81.3	(Hummel et al., 2002; Thoenen et al., 2013)
Calcite, $\text{C}_{\underline{\text{C}}}$	36.9	-1207	-1129	92.7	81.9	(Hummel et al., 2002; Thoenen et al., 2013)
Dolomite (disordered), $\text{CM}_{\underline{\text{C}}_2}$	64.4	-2317	-2157	167	158	(Hummel et al., 2002; Thoenen et al., 2013)
Natron, $\text{N}_{\underline{\text{C}}}\text{H}_{10}$	197	-4079	-3428	563	550	(Königsberger et al., 1999; Taga, 1969)
Gaylussite, $\text{NC}_{\underline{\text{C}}_2}\text{H}_5$	149	-3834	-3372	387	- ^d	(Dickens and Brown, 1969; Königsberger et al., 1999)
Pirssonite, $\text{NC}_{\underline{\text{C}}_2}\text{H}_2$	104	-2956	-2658	239	329	(Dickens and Brown, 1969; Königsberger et al., 1999)
Magnesite, $\text{M}_{\underline{\text{C}}}$	28.0	-1113	-1029	65.7	75.8	(Hummel et al., 2002; Thoenen et al., 2013)
Huntite, $\text{CM}_{\underline{\text{C}}_4}$	123	-4533	-4206	300	310	(Graf and Bradley, 1962; Hemingway and Robie, 1972; Königsberger et al., 1999)
Artinite, $\text{M}_{2\underline{\text{C}}}\text{H}_4$	96.2	-2921	-2568	233	248	(de Wolff, 1952; Hemingway and Robie, 1972; Königsberger et al., 1999)
Lansfordite, $\text{M}_{\underline{\text{C}}}\text{H}_5$	103	-2574	-2198	250	386	(Hill et al., 1982; Königsberger et al., 1999)
Zeolites						
Na-analcime, $[\text{Na}_{0.32} \cdot [\text{Al}_{0.32}\text{Si}_{0.68}\text{O}_2] \cdot 0.333\text{H}_2\text{O}]$	32.5 ^c	-1099	-1026	75.6	70.5	(Johnson et al., 1982)

Natrolite, $[\text{Na}_{0.4} \cdot [\text{Al}_{0.4} \text{Si}_{0.6} \text{O}_2] \cdot 0.4 \text{H}_2\text{O}$	33.8 ^c	-1144	-1063	71.9	60.4	(Johnson et al., 1983)
Ca-heulandite, $[\text{Ca}_{0.111} \cdot [\text{Al}_{0.222} \text{Si}_{0.778} \text{O}_2] \cdot 0.667 \text{H}_2\text{O}$	35.2 ^e	-1179	-1090	87.1	82.9	(Kiseleva et al., 2001)
(Ca,Na)-heulandite, $[\text{Ca}_{0.111} \text{Na}_{0.028}] \cdot [\text{Al}_{0.25} \text{Si}_{0.75} \text{O}_2] \cdot 0.667 \text{H}_2\text{O}$	35.2 ^e	-1185	-1094	84.0	82.9	(Kiseleva et al., 2001)
Basic sodalite, $[\text{Na}_{0.65} (\text{OH})_{0.15}] \cdot [\text{Al}_{0.5} \text{Si}_{0.5} \text{O}_2] \cdot 0.27 \text{H}_2\text{O}$	35.0 ^e	-1190	-1106	67.8 ^f	66.7 ^f	(Moloy et al., 2006)

198 ^a Cement chemistry notation is used: C = CaO; S = SiO₂; A = Al₂O₃; H = H₂O; N = Na₂O; M = MgO;
199 ^c = CO₂; ^s = SO₃.

200 ^b The asterisks for the T2C*, T5C* and TobH* end-members indicate that these components have
201 slightly modified thermodynamic properties but the same chemical composition relative to the T2C,
202 T5C and TobH end-members of the downscaled CSH3T thermodynamic model (Kulik, 2011).

203 ^c Thermodynamic properties based on the thermochemical data in (Allada et al., 2005) and solubility
204 data in (Bennett et al., 1992; Gao and Li, 2012), section 2.2, with molar volumes calculated from
205 (Richardson, 2013).

206 ^d Not available

207 ^e Molar volumes calculated from framework densities, lattice types and lattice cell parameters for each
208 zeolite framework type (Baerlocher et al., 2007).

209 ^f Standard entropy and heat capacity estimated using the additivity method (Anderson and Crerar,
210 1993) based on H₂O_(l) (Table 2), gibbsite (Helgeson et al., 1978; Hummel et al., 2002), NaOH_(s)
211 (Robie and Hemingway, 1995) and amorphous SiO₂ (Table 1).

212

213 Thermodynamic data for some zeolites and alkali carbonate minerals were used to provide a
214 preliminary assessment of the stability of these phases in AAS cements (Table 1) and should be
215 treated as provisional only, because the thermodynamic data were not recompiled for full internal
216 consistency with the Nagra-PSI and CEMDATA07 thermodynamic databases. Reliable
217 thermodynamic data for other Na-carbonates which can form in AAS cements (i.e. natrite,
218 thermonatrite, nahcolite and trona) were not available (Königsberger et al., 1999; Monnin and Schott,
219 1984), and so were not included in the simulations.

220

221 The formation of siliceous hydrogarnet was suppressed in the simulations because this phase does not
222 tend to form at ambient temperature and pressure, possibly for kinetic reasons (Lothenbach et al.,
223 2008). No additional restrictions related to the formation of any other solid phases shown in Table 1
224 were specified.

225

226 **2.5 Approach**

227 Thermodynamic modelling was performed using the Gibbs energy minimisation software GEM-
 228 Selektor v.3 (<http://gems.web.psi.ch/>) (Kulik et al., 2013; Wagner et al., 2012), with thermodynamic
 229 data for the solid phases shown in Table 1 and thermodynamic data for aqueous species/complexes
 230 and gases shown in Tables 2 and 3, respectively. The Truesdell-Jones form of the extended Debye-
 231 Hückel equation (eq.(3)) (Helgeson et al., 1981) and the ideal gas equation of state were used for the
 232 aqueous and gaseous phase models, respectively, with the average ion size (\bar{a} , Å) and the parameter
 233 for common short-range interactions of charged species (b_γ , kg mol⁻¹) specified to represent NaOH-
 234 dominated solutions (3.31 Å and 0.098 kg mol⁻¹, respectively (Helgeson et al., 1981)).

235

236

$$\log_{10} \gamma_j = \frac{-A_\gamma z_j^2 \sqrt{I}}{1 + \bar{a} B_\gamma \sqrt{I}} + b_\gamma I + \log_{10} \frac{x_{jw}}{X_w} \quad (3)$$

237

238 The parameters γ_j and z_j in eq.(3) are the activity coefficient and charge of the j^{th} aqueous species,
 239 respectively, A_γ (kg^{0.5} mol^{-0.5}) and B_γ (kg^{0.5} mol^{-0.5} cm⁻¹) are T,P-dependent electrostatic parameters, I
 240 is the ionic strength of the aqueous electrolyte phase (mol kg⁻¹), x_{jw} (mol) is the molar quantity of
 241 water and X_w (mol) is the total molar amount of the aqueous phase. The activity of water is calculated
 242 from the osmotic coefficient (Helgeson et al., 1981) and unity activity coefficients for neutral
 243 dissolved species are used.

244

245 Table 2. Thermodynamic properties of the aqueous species used in the thermodynamic modelling
 246 simulations.

Species/complex ^a	V° (cm ³ mol ⁻¹)	ΔH_f° (kJ mol ⁻¹)	ΔG_f° (kJ mol ⁻¹)	S° (J mol ⁻¹ K ⁻¹)	C_p° (J mol ⁻¹ K ⁻¹)	Reference
Al ³⁺	-45.2	-530.6	-483.7	-325.1	-128.7	(Shock et al., 1997)
AlO ⁺ (+ H ₂ O = Al(OH) ₂ ⁺)	0.3	-713.6	-660.4	-113	-125.1	(Shock et al., 1997)
AlO ₂ ⁻ (+ 2H ₂ O = Al(OH) ₄ ⁻)	9.5	-925.6	-827.5	-30.2	-49	(Shock et al., 1997)
AlOOH ^o (+ 2H ₂ O = Al(OH) ₃ ^o)	13	-947.1	-864.3	20.9	-209.2	(Shock et al., 1997)
AlOH ²⁺	-2.7	-767.3	-692.6	-184.9	56	(Shock et al.,

						1997)
AlHSiO ₃ ²⁺ (+ H ₂ O = AlSiO(OH) ₃ ²⁺)	-40.7	-1718	-1541	-304.2	-215.9	(Matschei et al., 2007)
AlSiO ₄ ⁻ (+ 3H ₂ O = AlSiO(OH) ₆ ⁻)	25.5	-1834	-1681	11.1	-4.6	(Matschei et al., 2007)
AlSO ₄ ⁺	-6.0	-1423	-1250	-172.4	-204.0	(Matschei et al., 2007)
Al(SO ₄) ₂ ⁻	31.1	-2338	-2006	-135.5	-268.4	(Matschei et al., 2007)
Ca ²⁺	-18.4	-543.1	-552.8	-56.5	-30.9	(Shock et al., 1997)
CaOH ⁺	5.8	-751.6	-717	28	6	(Shock et al., 1997)
CaHSiO ₃ ⁺ (+ H ₂ O = CaSiO(OH) ₃ ⁺)	-6.7	-1687	-1574	-8.3	137.8	(Sverjensky et al., 1997)
CaSiO ₃ ^o (+ H ₂ O = CaSiO ₂ (OH) ₂ ^o)	15.7	-1668	-1518	-136.7	88.9	(Matschei et al., 2007)
CaSO ₄ ^o	4.7	-1448	-1310	20.9	-104.6	(Sverjensky et al., 1997)
CaCO ₃ ^o	-1.6	-1202	-1099	10.5	-123.9	(Sverjensky et al., 1997)
CaHCO ₃ ⁺	13.3	-1232	-1146	66.9	233.7	(Hummel et al., 2002; Thoenen et al., 2013)
K ⁺	9.0	-252.1	-282.5	101	8.4	(Shock et al., 1997)
KOH ^o	15	-474.1	-437.1	108.4	-85	(Shock et al., 1997)
KSO ₄ ⁻	27.5	-1159	-1032	146.4	-45.1	(Sverjensky et al., 1997)
Na ⁺	-1.2	-240.3	-261.9	58.4	38.1	(Shock et al., 1997)
NaOH ^o	3.5	-470.1	-418.1	44.8	-13.4	(Shock et al., 1997)
NaSO ₄ ⁻	18.6	-1147	-1010	101.8	-30.1	(Matschei et al., 2007)
NaCO ₃ ⁻	-0.4	-938.6	-797.1	-44.3	-51.3	(Hummel et al., 2002; Thoenen et al., 2013)
NaHCO ₃ ^o	32.3	-929.5	-847.4	154.7	200.3	(Hummel et al., 2002; Thoenen et al., 2013)
HSiO ₃ ⁻ (+ H ₂ O = SiO(OH) ₃ ⁻)	4.5	-1145	-1014	20.9	-87.2	(Sverjensky et al., 1997)
SiO ₂ ^o (+ 2H ₂ O = Si(OH) ₄ ^o)	16.1	-887.9	-833.4	41.3	44.5	Kulik and Kersten, 2001; Shock et al., 1989)
SiO ₃ ²⁻ (+ H ₂ O = SiO ₂ (OH) ₂ ²⁻)	34.1	-1099	-938.5	-80.2	119.8	(Matschei et al., 2007)
S ₂ O ₃ ²⁻	27.6	-649.9	-520.0	66.9	-238.5	(Shock et al., 1997)
HSO ₃ ⁻	33.0	-627.7	-529.1	139.7	-5.4	(Shock et al., 1997)
SO ₃ ²⁻	-4.1	-636.9	-487.9	-29.3	-281.0	(Shock et al.,

						1997)
HSO ₄ ⁻	34.8	-889.2	-755.8	125.5	22.7	(Shock et al., 1997)
SO ₄ ²⁻	12.9	-909.7	-744.5	18.8	-266.1	(Shock et al., 1997)
H ₂ S ^o	35.0	-39.0	-27.9	125.5	179.2	(Shock et al., 1997)
HS ⁻	20.2	-16.2	12.0	68.2	-93.9	(Shock et al., 1997)
S ²⁻	20.2	92.2	120.4	68.2	-93.9	(Shock et al., 1997)
Mg ²⁺	-22.0	-465.9	-454.0	-138.1	-21.7	(Shock et al., 1997)
MgOH ⁺	1.6	-690.0	-625.9	-79.9	129.2	(Shock et al., 1997)
MgHSiO ₃ ⁺ (+ H ₂ O = MgSiO(OH) ₃ ⁺)	-10.9	-1614	-1477	-99.5	158.6	(Shock et al., 1997)
MgSO ₄ ^o	1.8	-1369	-1212	-50.9	-90.3	(Hummel et al., 2002; Shock et al., 1997; Thoenen et al., 2013)
MgSiO ₃ ^o (+ H ₂ O = MgSiO ₂ (OH) ₂ ^o)	12.1	-1597	-1425	-218.3	98.2	(Hummel et al., 2002; Thoenen et al., 2013)
MgCO ₃ ^o	-16.7	-1132	-999.0	-100.4	-116.5	(Sverjensky et al., 1997; Thoenen et al., 2013)
MgHCO ₃ ⁺	9.3	-1154.0	-1047	-12.6	254.4	(Hummel et al., 2002; Thoenen et al., 2013)
CO ₂ ^o	32.8	-413.8	-386.0	117.6	243.1	(Hummel et al., 2002; Shock et al., 1989; Thoenen et al., 2013)
CO ₃ ²⁻	-6.1	-675.3	-528.0	-50.0	-289.3	(Shock et al., 1997)
HCO ₃ ⁻	24.2	-690.0	-586.9	98.5	-34.8	(Shock et al., 1997)
CH ₄ ^o	37.4	-87.8	-34.4	87.8	277.3	(Hummel et al., 2002; Shock and Helgeson, 1990; Thoenen et al., 2013)
OH ⁻	-4.7	-230	-157.3	-10.7	-136.3	(Shock et al., 1997)
H ⁺	0	0	0	0	0	(Shock et al., 1997)
H ₂ O ^o	18.1	-285.9	-237.2	69.9	75.4	(Johnson et al., 1992)
H ₂ ^o	25.3	-4.0	17.7	57.7	166.9	(Hummel et al.,

							2002; Shock et al., 1989; Thoenen et al., 2013)
	N ₂ ^o	33.4	-10.4	18.2	95.8	234.2	(Shock et al., 1989)
	O ₂ ^o	30.5	-12.2	16.4	109	234.1	(Shock et al., 1989)

247 ^a The hydration reactions shown in parentheses indicate hydrated species/complexes represented by
 248 the simulated aqueous species/complexes.

249

250 Table 3. Thermodynamic properties of the gases used in the thermodynamic modelling simulations.

Gases	V° (cm ³ mol ⁻¹)	ΔH _f ^o (kJ mol ⁻¹)	ΔG _f ^o (kJ mol ⁻¹)	S° (J mol ⁻¹ K ⁻¹)	Cp° (J mol ⁻¹ K ⁻¹)	Reference
N ₂	24790	0	0	191.6	29.1	(Wagman et al., 1982)
O ₂	24790	0	0	205.1	29.3	(Wagman et al., 1982)
H ₂	24790	0	0	130.7	28.8	(Wagman et al., 1982)
CO ₂	24790	-393.5	-394.4	213.7	37.1	(Wagman et al., 1982)
CH ₄	24790	-74.8	-50.7	186.2	35.7	(Wagman et al., 1982)
H ₂ S	24790	-20.6	-33.8	205.8	34.2	(Wagman et al., 1982)

251

252

253 Chemical equilibrium between the solid, aqueous and gaseous phases was assumed, and the simulated
 254 slag was specified to dissolve congruently at each particular bulk slag chemical composition. The
 255 assumption of congruent dissolution is valid for calcium aluminosilicate glasses of similar bulk
 256 chemical compositions to GBFS in highly under-saturated conditions at pH = 13 (Snellings, 2013).

257 This condition is likely to be approximated in AAS cements when the solution pH is sufficiently high
 258 (Bernal et al., 2015), although it is clear that this assumption will need to be revisited in some
 259 systems, particularly for AAS cements cured for long times or synthesised with less basic activators
 260 such as N_c (Bernal et al., 2015).

261

262 Simulations of AAS cements were performed using 100 g slag, additions of H₂O, NaOH or Na₂O,
 263 SiO₂ and Na₂CO₃ to achieve fixed water to binder (w/b, where binder = slag + anhydrous activator

264 component) ratios of 0.4 and activator concentrations of 4 g Na₂O equivalent/100 g slag (the
265 activators used are NaOH, Na₂SiO₃, Na₂Si₂O₅ and Na₂CO₃), a nitrogen atmosphere (10 mol N₂(g) per
266 100 g slag), and temperature/pressure conditions of 298.15 K and 1 bar. This simulation setup directly
267 represents the AAS cements studied in (Bernal et al., 2015; Bernal et al., 2014b; Myers et al., 2015a;
268 Myers et al., 2013), and is also similar to the AAS cement formulations reported in (Ben Haha et al.,
269 2011b, 2012; Le Saoût et al., 2011) (which had ~3 mass% Na₂O equivalent and w/b = 0.4). With the
270 exception of the phase diagram simulations (section 3.4), the simulated slag compositions are based
271 on the GBFS composition shown in Table 4.

272

273 Table 4. Bulk chemical composition of the GBFS (from (Myers et al., 2015a)) used to specify the
274 chemical compositions of the simulated slag in the thermodynamic modelling simulations.

Component	Chemical composition (mass%)
SiO ₂	33.8
CaO	42.6
MgO	5.3
Al ₂ O ₃	13.7
Na ₂ O	0.1
K ₂ O	0.4
SO ₃ ^a	0.8
Other	1.5
LOI ^b	1.8
Total	100

275 ^a S is represented in oxide form in standard XRF analysis, but S is treated as S²⁻ here (see section 2.2).

276 ^b LOI is loss on ignition at 1000°C.

277

278 In section 3.1, the utility of the thermodynamic database (Tables 1-3) is assessed by using the slag
279 composition given in Table 4 in terms of SiO₂, CaO, MgO, Al₂O₃, Na₂O, K₂O, and H₂S
280 (corresponding to the “SO₃” content of the slag in Table 4) only, except for a variable oxide
281 component (Al₂O₃, MgO or CaO), which was specified according to the simulation conducted. A
282 simulated slag reaction extent of 60% was employed, which represents a typical degree of reaction
283 quantified for GBFS in sodium silicate-activated slag cements (~48% at 180 days in (Ben Haha et al.,
284 2011a), 54 ±3% at 100 days in (Le Saoût et al., 2011), 58-61% at 180 days in (Bernal et al., 2014b)
285 and >70% after 1 month in (Myers et al., 2015a)). A density of 2.8 g/cm³ was selected for the
286 unreacted slag component (Bernal et al., 2015).

287

288 Specific details pertaining to the descriptions of the slags simulated here, for each other aspect of the
289 study, are shown near the beginning of each of sections 3.2-3.4.

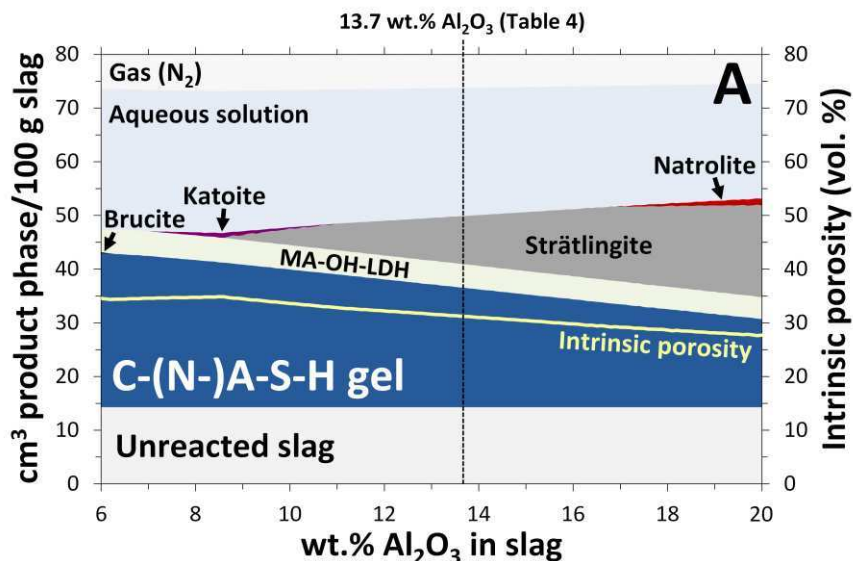
290

291 **3. Results and discussion**

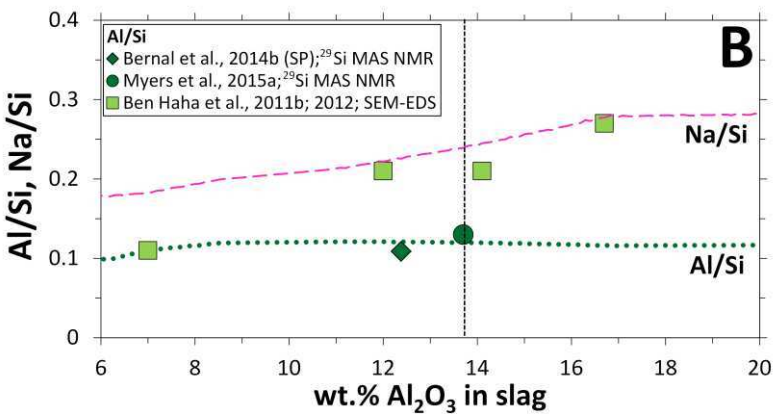
292 **3.1 Utility of the CNASH_ss and MA-OH-LDH_ss thermodynamic models**

293 Figure 2A shows that the calculated phase assemblage in NS-activated slag (NS-AS) cement changes
294 as a function of Al_2O_3 content in the slag. The phase assemblage is dominated by C-(N)-A-S-H gel, in
295 addition to MA-OH-LDH at all Al_2O_3 contents, and strätlingite, which also forms between 9 and 20
296 mass% Al_2O_3 . Mg-Al LDH phases are commonly identified in sodium silicate-activated slag cements
297 derived from slags with ≥ 5 mass% MgO (Bernal et al., 2014b), in good agreement with these results;
298 LDH formation is reassessed in detail below. The simulated volume of the MA-OH-LDH phase does
299 not change greatly here because its formation is limited by the amount of Mg supplied by the slag,
300 which is constant at a fixed slag reaction extent. Small amounts of katoite are predicted for slags with
301 7-11 mass% Al_2O_3 , which is relatively consistent with the observation of small amounts of this phase
302 in sodium silicate-activated slag cements produced from slags with ~ 13 mass% Al_2O_3 (Bernal et al.,
303 2014b; Schneider et al., 2001). Natrolite is predicted between 17 and 20 mass% slag Al_2O_3 content
304 and very small quantities of brucite are predicted for slags with < 7 mass% Al_2O_3 .

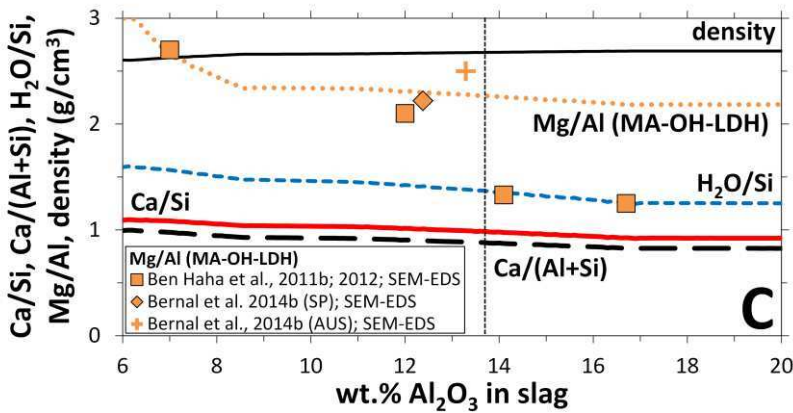
305



306



307



308

309 Figure 2. Simulated A) solid phase assemblages, B) Al/Si ratios in C-(N)-A-S-H gel, and C) Mg/Al
 310 ratios in MA-OH-LDH in NS-AS cements with bulk slag chemical compositions rescaled from Table
 311 4 except for the Al₂O₃ content, which is varied here. Changes in B) Na/Si, C) H₂O/Si, Ca/Si and
 312 Ca/(Al+Si) ratios in C-(N)-A-S-H gel, and C) C-(N)-A-S-H gel density (g/cm³) are shown for visual
 313 reference. The symbols in B) and C) are experimental results for sodium silicate-activated slag
 314 cements cured for 180 days and derived from slag precursors with similar MgO and equivalent or
 315 slightly lower CaO content (5.2 < mass% MgO < 7.7, 35 < mass% CaO ≤ 42.6) to the slag
 316 represented by Table 4.

317

318 The Mg/Al ratio of the simulated MA-OH-LDH phase is between 2 and 3 over the full range of
319 simulated slag Al_2O_3 compositions (Figure 2C), in excellent agreement with experimentally
320 determined Mg/Al ratios for this phase by scanning electron microscopy (SEM) with energy-
321 dispersive X-ray spectroscopy (EDS) analysis in sodium silicate-activated slag cements for slags
322 containing $7 \leq \text{mass}\% \text{ Al}_2\text{O}_3 \leq 13.3$ (Ben Haha et al., 2012; Bernal et al., 2014b). However, the
323 experimental SEM-EDS data suggest a systematic reduction in the Mg/Al ratio of this phase to below
324 2 as a function of increasing slag Al_2O_3 content (Ben Haha et al., 2012; Bernal et al., 2014b), that was
325 not captured by the modelling performed here, as the MA-OH-LDH_ss thermodynamic model only
326 describes solid solutions in the range $2 \leq \text{Mg/Al} \leq 4$. Regions with Mg/Al ratios < 2 identified in
327 transmission electron microscopy (TEM)-EDS analysis of hydrated PC/GBFS cements (Taylor et al.,
328 2010) are discussed in terms of intimate mixtures of Mg-Al LDH and Al(OH)_3 -type phases because
329 the chemical composition of Mg-Al LDH is theoretically limited to the range modelled here, $2 \leq$
330 $\text{Mg/Al} \leq 4$ (Richardson, 2013). The experimental Mg/Al ratios < 2 shown in Figure 2C can thus be
331 described similarly, which would explain the difference between the modelled and experimentally
332 measured data. This analysis suggests a need for additional thermodynamic data describing Al-rich
333 and Mg-poor solid phases that are not currently included in the thermodynamic database (e.g. TAH
334 (Andersen et al., 2006)) rather than a deficiency in the MA-OH-LDH_ss thermodynamic model as
335 such.

336

337 The amount of C-(N)-A-S-H gel formed in the simulated NS-AS cements decreases with increasing
338 Al_2O_3 content of the slag (Figure 2A) at the expense of strätlingite precipitation. An Al/Si ratio ≈ 0.12
339 is calculated for C-(N)-A-S-H gel in NS-AS cements derived from slags with >8 mass% Al_2O_3
340 (Figure 2B), which corresponds closely to the Al/Si ratios determined for this phase by analysis of
341 deconvoluted ^{29}Si magic angle spinning nuclear magnetic resonance (MAS NMR) spectra for these
342 materials at 180 days of age (Bernal et al., 2014b; Myers et al., 2015a) using the CSTM (Myers et al.,
343 2013). The CSTM is a structural model that represents C-(N)-A-S-H gel in terms of mixed cross-
344 linked/non-cross-linked components that enables chemical compositions and structural parameters to
345 be determined from deconvolution analysis of ^{29}Si MAS NMR spectra for materials containing this

346 phase. However, the experimental Al/Si ratios determined from ^{29}Si MAS NMR shown here exclude
347 the potential uptake of Al[5] (Andersen et al., 2006) and Al[6] (Sun et al., 2006) in C-(N-)A-S-H gel,
348 so are expected to be slightly lower than the ‘true’ Al/Si ratio in this phase. This discrepancy is
349 discussed further in section 3.2. However, the much higher Al/Si ratios shown by the other SEM-EDS
350 data, with Mg/Al < 2, could indicate mixtures of C-(N-)A-S-H gel with Mg-free and Al-containing
351 phases in the interaction volumes analysed by SEM-EDS. This description is similar to the analysis
352 above for Mg-Al LDH, so the thermodynamic modelling results are not necessarily inconsistent with
353 these experimental SEM-EDS data.

354

355 The total binder volume (solid + aqueous phases) is calculated to be approximately constant over the
356 full range of slag Al_2O_3 compositions studied (Figure 2A), suggesting that the bulk Al content of the
357 slag in NS-AS cements should not greatly affect the chemical shrinkage properties of these materials.
358 The results indicate a 20% change in intrinsic porosity (defined as the ratio of aqueous phase volume
359 to total binder volume, where water chemically bound in, or adsorbed to, the solid phases described in
360 Table 1 is considered to be a component of the solid) for slag compositions between ~8 and 20 mass%
361 Al_2O_3 . This interpretation corresponds to the simulated C-(N-)A-S-H gel density of 2.5-2.7 g/cm³ and
362 $\text{H}_2\text{O}/\text{Si}$ ratios between 1.3 and 1.7 (in agreement with C-(N-)A-S-H gel at RH ≈ 25% (Muller et al.,
363 2013)), as shown in Figure 2C. Therefore, this phase is conceptually equivalent to C-(N-)A-S-H gel
364 with interlayer and some adsorbed water but no ‘gel’ or ‘free’ water (Jennings, 2008). However, the
365 reduced intrinsic porosity found here at higher bulk slag Al_2O_3 content does not explain the weak
366 dependency of sodium silicate-activated slag cement compressive strengths on bulk slag Al_2O_3
367 content (Ben Haha et al., 2012), because an increase in compressive strength would be expected at
368 lower porosity. This discrepancy is attributed to the higher amount of strätlingite simulated here
369 compared to the amount of this phase which is identified in AAS cements; this issue is revisited in
370 section 3.2.

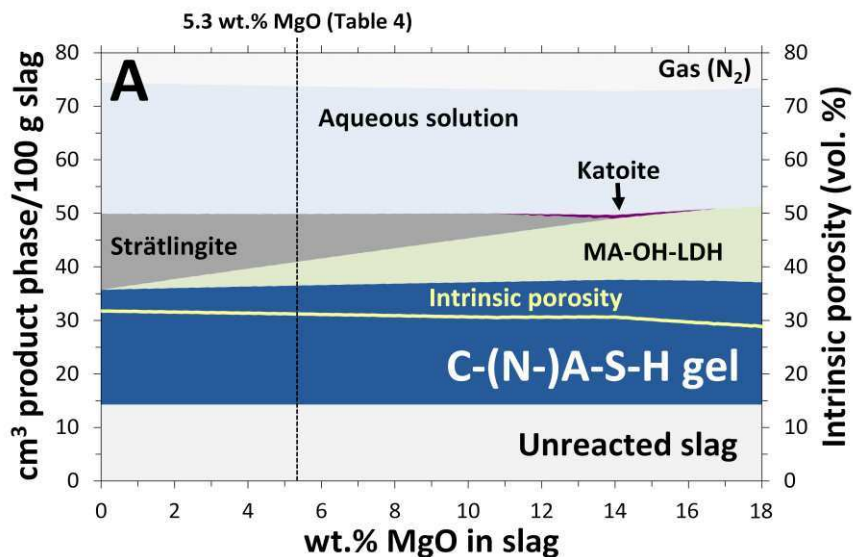
371

372 Simulations of NS-AS cements derived from slags with 0-18 mass% MgO (Figure 3) show little
373 change in intrinsic porosity and total binder volume as a function of MgO content. This result differs

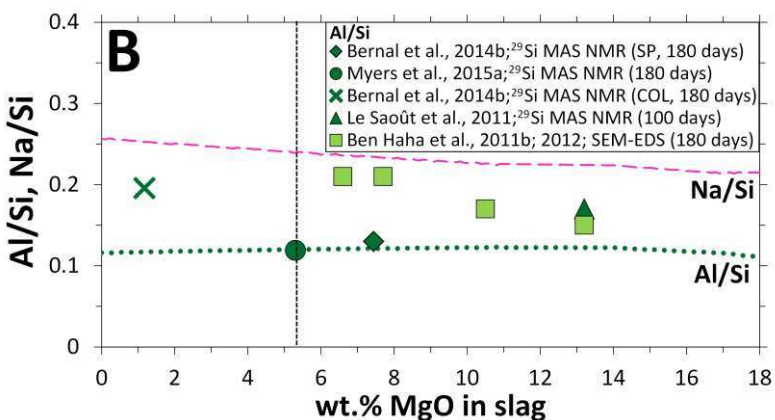
374 from previous thermodynamic modelling that showed a significant increase in total solid volume over
375 this same MgO composition range (Ben Haha et al., 2011b). This difference is partly founded in the
376 high amounts of strätlingite predicted, but also relates to the use of the CNASH_ss thermodynamic
377 model here, rather than the less complex thermodynamic model used to describe C-(N-)A-S-H gel by
378 Ben Haha et al. (2011b) (density \approx 2.2-2.4 g/cm³ (Lothenbach et al., 2008)), as the current work
379 formally defines the uptake of Al in C-(N-)A-S-H gel and much more closely describes the volumetric
380 properties of this phase in sodium silicate-activated slag cement (density = 2.6-2.7 g/cm³ in Figure
381 3C, compared to 2.73 ± 0.02 g/cm³ reported by Thomas et al. (2012)).

382

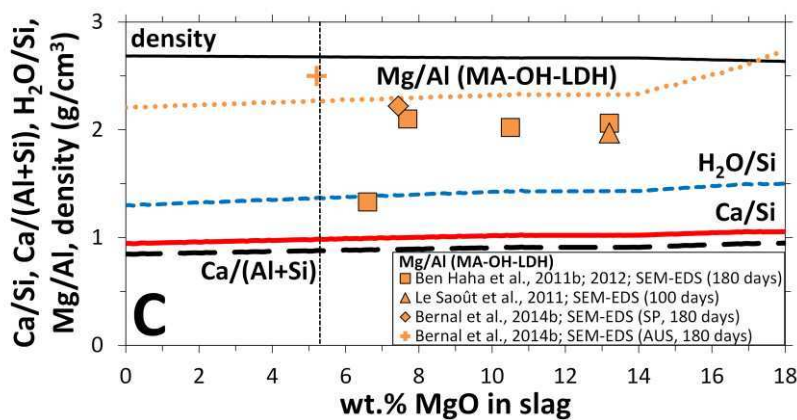
383



384



385



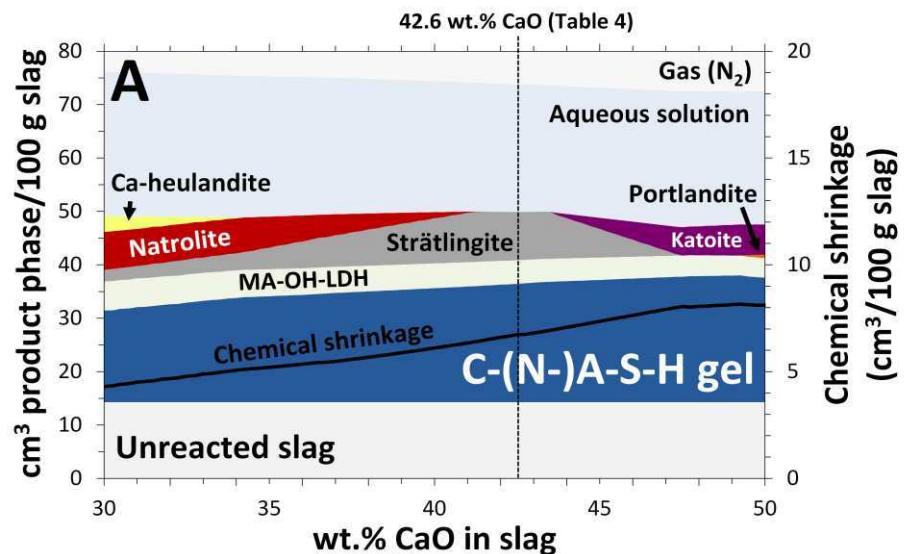
386

387 Figure 3. Simulated A) solid phase assemblages, B) Al/Si ratios in C-(N)-A-S-H gel, and C) Mg/Al
 388 ratios in MA-OH-LDH in NS-AS cements with bulk slag chemical compositions rescaled from Table
 389 4 except for the Mg content, which is varied here. Changes in B) Na/Si, C) H₂O/Si, Ca/Si and
 390 Ca/(Al+Si) ratios in C-(N)-A-S-H gel, and C) C-(N)-A-S-H gel density (g/cm³) are shown for visual
 391 reference. The symbols in B) and C) represent experimentally measured data for sodium silicate-
 392 activated slag cements (curing times are indicated in parentheses) derived from slag precursors with
 393 similar Al₂O₃ and equivalent or slightly lower CaO content (11.3 < mass% Al₂O₃ < 14.1, 33.4 <
 394 mass% CaO ≤ 42.6) to the slag represented by Table 4.
 395

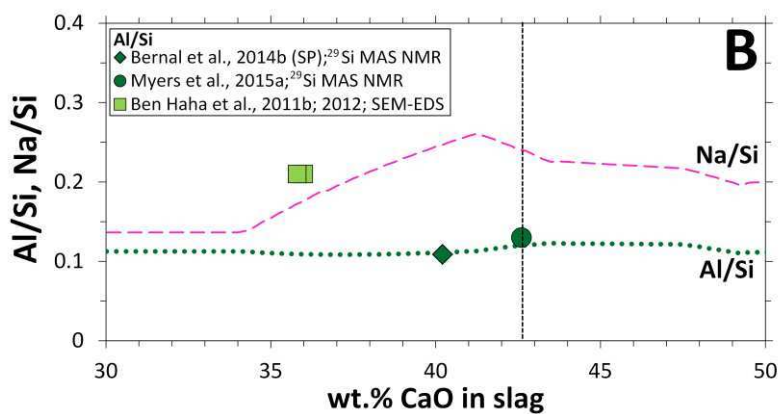
396 The solid phase assemblage changes markedly as a function of the MgO content of the slag (Figure
397 3A), but little change in C-(N)-A-S-H gel volume is simulated between 0 and 18 mass% MgO. The
398 only Mg-bearing solid phase predicted is MA-OH-LDH, the amount of which increases as a function
399 of the slag MgO content. The simulated and experimentally measured Mg/Al ratios of this phase in
400 sodium silicate-activated slag cements are consistent to ± 0.3 units (simulated Mg/Al ≈ 2.3 , Figure 3C)
401 (Ben Haha et al., 2011b; Bernal et al., 2014b; Le Saoût et al., 2011), with the exception of the samples
402 containing significant intermixing of additional products (with Mg/Al $\ll 2$). This result further
403 supports the thermodynamic description of MA-OH-LDH used here. The only predicted minor phase
404 is katoite at 11-17 mass% MgO. Brucite is not predicted here, in good agreement with its absence
405 from experimentally observed solid phase assemblages in AAS cements (Ben Haha et al., 2011b;
406 Myers et al., 2015a; Richardson et al., 1994; Schneider et al., 2001; Wang and Scrivener, 1995).

407

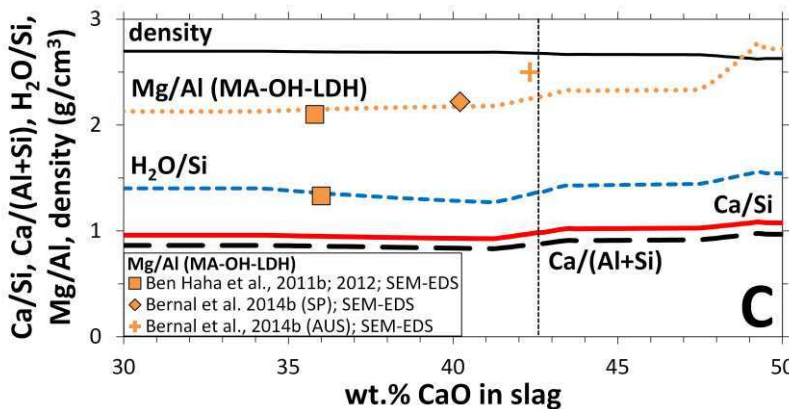
408 The Al/Si ratio of the simulated C-(N)-A-S-H gel ($\text{Al/Si} \approx 0.12$) is similar to the experimentally
409 determined Al content of this phase in sodium silicate-activated slag cements derived from slags with
410 $13.2 \geq \text{mass\% MgO}$ (Bernal et al., 2014b; Le Saoût et al., 2011) (Figure 3B), except for the SEM-
411 EDS datum at ~ 7.8 mass% MgO (Ben Haha et al., 2012) and the ^{29}Si MAS NMR datum at 1.2 mass%
412 MgO ($\text{Al/Si} \approx 0.2$) (Bernal et al., 2014b). This discrepancy can be partly attributed to the incomplete
413 description of solid phases in the thermodynamic database, which would be particularly relevant for
414 the datum at 1.2 mass% MgO, as gismondine and/or N-A-S(-H) gel (which is thought to be a poorly-
415 ordered zeolite-type phase (Provis et al., 2005)) were identified as reaction products in the cement
416 studied by Bernal et al. (2014b). Simulations of NS-AS cements show that Ca-heulandite and natrolite
417 are predicted for slags with ≤ 41 mass% CaO (Figure 4), in good agreement with this analysis and the
418 identification of zeolites in these materials (Bernal et al., 2011; Bernal et al., 2014b). The bulk CaO
419 concentration is therefore a key parameter controlling the formation of zeolite-type phases in AAS-
420 based cements. However, it is important to note that Ca-rich zeolites such as gismondine, which are
421 expected to have relatively high stability in AAS-based cements, are not described in the
422 thermodynamic database used here because reliable thermodynamic data for these phases are not
423 always available (Wolery et al., 2007).



424



425



426

Figure 4. Simulated A) solid phase assemblages, B) Al/Si ratios in C-(N)-A-S-H gel, and C) Mg/Al ratios in MA-OH-LDH in NS-AS cements with bulk slag chemical compositions rescaled from Table 4 except for the Ca content, which is varied here (traces). Changes in B) Na/Si, C) H₂O/Si, Ca/Si and Ca/(Al+Si) ratios in C-(N)-A-S-H gel, and C) C-(N)-A-S-H gel density (g/cm³) are shown for visual reference. The symbols in B) and C) represent experimentally measured data for sodium silicate-activated slag cements derived from slag precursors with similar Al₂O₃ and MgO content (12 < mass% Al₂O₃ < 14.1, 5.2 < mass% MgO < 7.7) to the slag represented by Table 4. The difference in intrinsic porosity within the full range of modelled CaO compositions is 3%.

436 It is also notable that the total binder (solid + aqueous phase) volume changes markedly as a function
437 of the CaO content in the slag, which suggests that the bulk CaO concentration is also a key parameter
438 influencing the chemical shrinkage properties of these materials; a difference of $3.8 \text{ cm}^3/100 \text{ g}$ slag
439 ($\Delta\text{chemical shrinkage} = 47\%$) is identified over the range $30 \leq \text{CaO} \leq 49$ mass%, with more chemical
440 shrinkage predicted at higher slag CaO content (Figure 4A). Therefore, it is expected that chemical
441 shrinkage in NS-AS cements can be reduced through the use of raw materials with lower CaO
442 content. Simulated Mg/Al ratios of the MA-OH-LDH phase and Al/Si ratios of C-(N-)A-S-H gel are
443 in close agreement with the experimental data, with the exception of the SEM-EDS data at a slag CaO
444 content of ~36 mass% which likely contains some intermixed low-Mg high-Al phases (Taylor et al.,
445 2010).

446

447 The modelling results presented here provide a satisfactory account of the experimental data and so
448 give confidence in using the CNASH_ss and MgAl-OH_LDH_ss thermodynamic models to describe
449 NS-AS cements over the most common ranges of slag compositions and activator doses used in AAS
450 cements ($7 \leq \text{mass\% Al}_2\text{O}_3 \leq 13.7$, Figure 2, $5.2 \leq \text{mass\% MgO} \leq 13.2$, Figure 3, and $35.8 \leq \text{mass\%}$
451 $\text{CaO} \leq 42.3$, Figure 4). Within this range, the model predictions are within ~0.04 units in the Al/Si
452 ratios of the C-(N-)A-S-H gel and ~0.3 units in the Mg/Al ratios of the MA-OH-LDH phase.

453

454 3.2 Simulated reaction of a Na_2SiO_3 -activated slag cement

455 Additional thermodynamic modelling analysis of NS-AS cements was performed by varying the slag
456 reaction extent from 0-100%, in the presence of Na_2SiO_3 (8 g $\text{Na}_2\text{SiO}_3/100 \text{ g}$ slag), while holding the
457 slag chemical composition constant (Table 4).

458

459 The predicted solid phase assemblage consists of C-(N-)A-S-H gel as the dominant reaction product,
460 and additionally MA-OH-LDH ($\text{Mg/Al} \approx 2$), strätlingite, Ca-heulandite, brucite, natrolite and katoite
461 (Figure 5A). Zeolites are only predicted for slag reaction extents <40% (i.e. effectively at low bulk
462 CaO concentrations, consistent with Figure 4), which is less than the experimentally-determined slag

463 reaction extent for AAS cement after 1 day of curing (Myers et al., 2015a), and is relatively consistent
464 with the experimental observation of only minor amounts of these phases in AAS cements (Bernal et
465 al., 2011; Bernal et al., 2014b).

466

467 The prediction of MA-OH-LDH and strätlingite is in relatively good agreement with experimentally-
468 determined solid phase assemblages in NS-AS cements (Ben Haha et al., 2012; Brough and Atkinson,
469 2002; Burciaga-Díaz and Escalante-García, 2013; Myers et al., 2015a; Wang and Scrivener, 1995),
470 where Mg-Al LDH phases are often identified and the formation of AFm-type phases are likely,
471 although the calculations here do markedly over-predict the amount of strätlingite formed compared
472 to the experimental observations. Approximately constant proportions of the main hydrate phases
473 (strätlingite, MA-OH-LDH and C-(N-)A-S-H gel) are predicted relative to the total reaction product
474 volume at slag reaction extents exceeding 40%. The influence of the additional Si supplied by the
475 activator is diluted as more slag reacts, as the activator is assumed to be fully dissolved in the mix
476 water prior to contact with the slag, and so contributes more significantly to the chemistry of the
477 reaction products when the degree of reaction of the slag is low. This means that the slag chemical
478 composition, rather than the activator, controls the stable product phase assemblage at higher extents
479 of reaction.

480

481 The chemical shrinkage in this system is predicted to be 11 cm³/100 g slag at complete reaction of the
482 slag (an overall volume reduction of 15%, Figure 5A), which matches the chemical shrinkage
483 quantified experimentally by Thomas et al. (2012) for a sodium silicate-activated slag cement (12.2 ±
484 1.5 cm³/100 g slag) and is close to the values modelled by Chen and Brouwers (2007) (11.5-13.9
485 cm³/100 g slag) at 100% degree of reaction of the slag. Therefore, thermodynamic modelling predicts
486 significantly larger chemical shrinkage in NS-AS cements than measured in hydrated PC (~6 cm³/100
487 g cement reacted (Jensen and Hansen, 2001; Tazawa et al., 1995)).

488

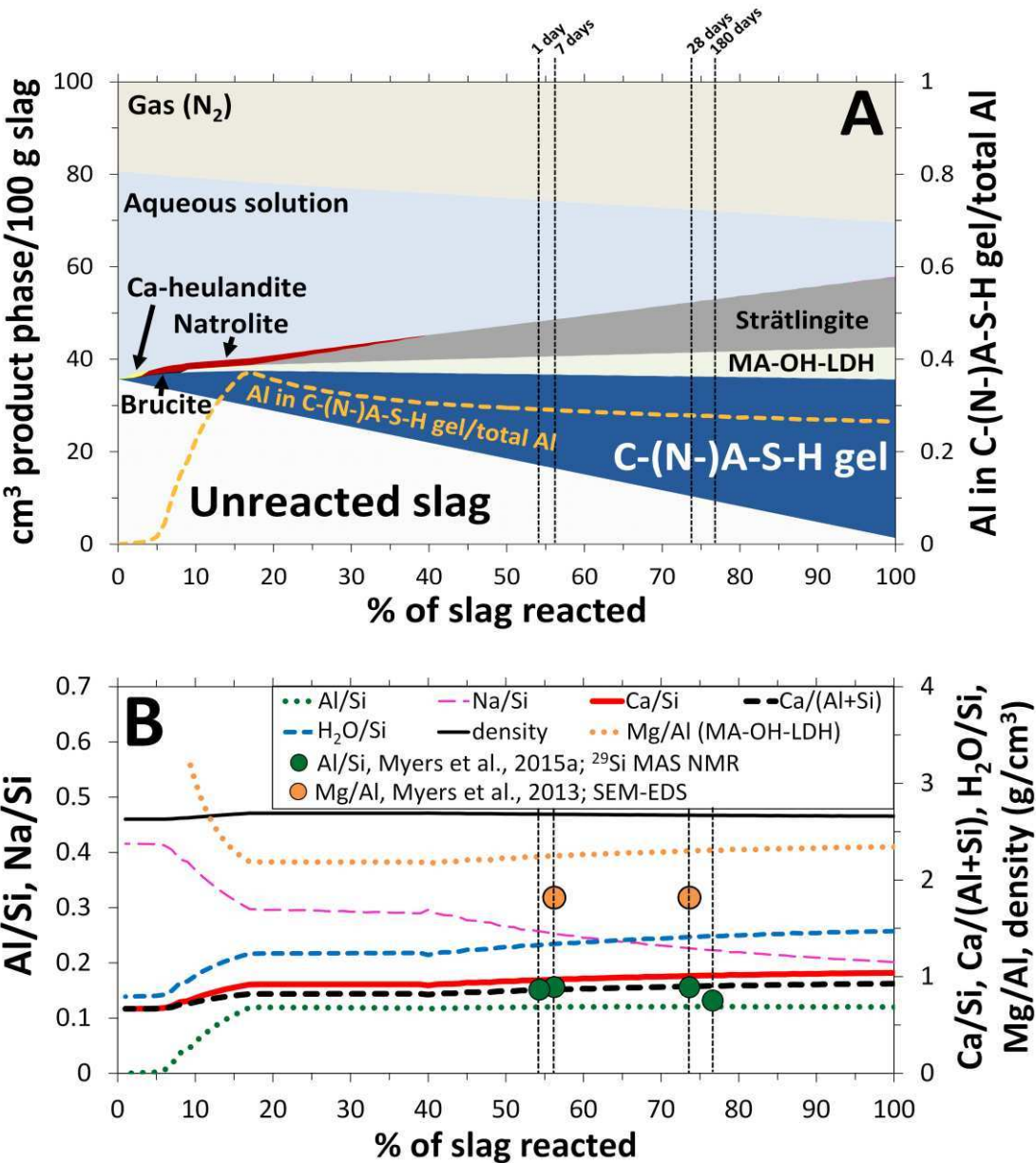


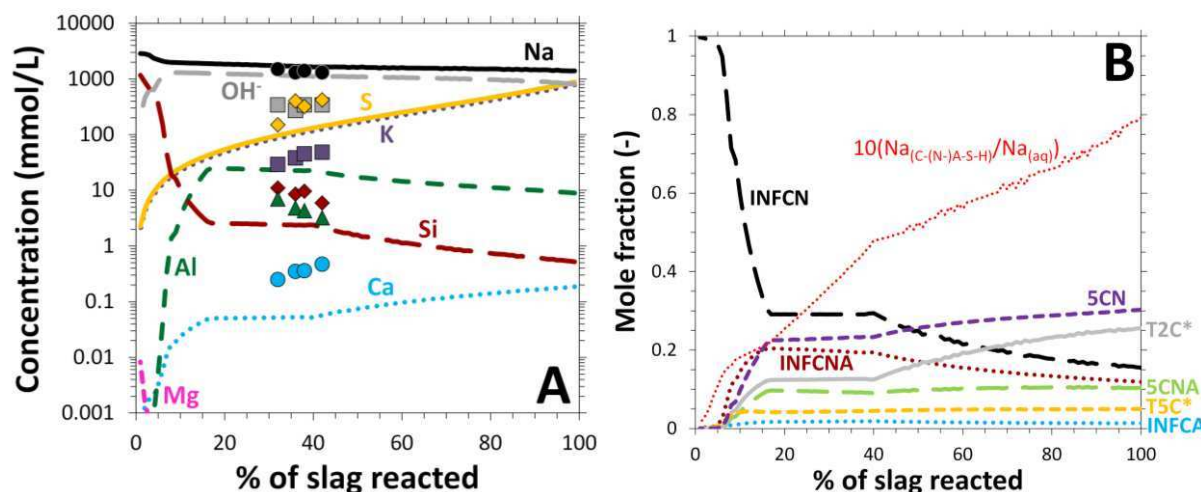
Figure 5. Simulated A) solid phase assemblages, and B) Al/Si ratios in C-(N-)A-S-H gel and Mg/Al ratios in MA-OH-LDH in an NS-AS cement using the slag chemical composition in Table 4. Changes in B) Na/Si, H₂O/Si, Ca/Si and Ca/(Al+Si) ratios in C-(N-)A-S-H gel, and B) C-(N-)A-S-H gel density (g/cm³) are shown for visual reference. The dashed vertical lines correspond to slag reaction extents determined experimentally at each time of curing (Myers et al., 2015a).

490
491
492
493
494
495
496

497 The increased Ca content and decreased Na/Si ratio of the C-(N-)A-S-H gel at higher slag reaction
498 extents (Figure 5B) are reflected in the reduced bulk Si and Na concentrations and the relative
499 decrease in the fraction of Na-containing end-members simulated as the alkali activation reaction
500 progresses (Figure 6). A ~50% reduction in the concentration of Na in the pore solution is predicted
501 from 0 to 100% slag reaction extent, although a constant pH of ~14 is maintained and >10 times more
502 Na is always predicted to be present in the aqueous phase relative to C-(N-)A-S-H gel. The simulated

503 amounts of H₂O and Ca in C-(N)-A-S-H gel are directly linked via the end-member chemical
 504 compositions defined in the CNASH_ss thermodynamic model (Myers et al., 2014): the Ca-rich T2C*
 505 end-member (Ca/Si = 1.5) has a higher H₂O/Si ratio (= 2.5) compared to the Al and Na-containing
 506 end-members (H₂O/Si < 2, Table 1), and relatively more of this end-member is simulated at higher
 507 bulk slag reaction extents (Figure 6B). The simulated trends in pore solution element concentrations at
 508 >40% slag reaction extent (Figure 6A) are within ± 1 order of magnitude to those reported for NS-AS
 509 cement cured for 1-180 days (Gruskovnjak et al., 2006). More solubility data for NS-AS cement are
 510 needed to further assess the simulated pore solution compositions.

511



512
 513 Figure 6. Simulated A) pore solution chemical compositions and B) end-member mole fractions and
 514 ratio of Na in C-(N)-A-S-H gel relative to Na in the aqueous phase (aq) for the NS-AS cement
 515 described by Figure 5. The mole fraction of the TobH* end-member is close to 0 over the full range of
 516 simulated slag reaction extents (not shown in B)). The symbols in A) represent sodium silicate-
 517 activated slag pore solution data reported by Gruskovnjak et al. (2006).

518

519 The simulated fraction of Al in MA-OH-LDH relative to the total amount of Al in the reaction
 520 products ($Al_{MgAl} LDH / Al_{products}$) is ~0.22, which is consistent with deconvolution analysis of ²⁷Al MAS
 521 NMR spectra for the analogous experimental NS-AS cement between 1-180 days of curing (Al_{MgAl}
 522 $LDH / Al_{products} = 0.18-0.26$) (Myers et al., 2015a), but the predicted Mg/Al ratios are greater than those
 523 measured by SEM-EDS analysis for this material (Figure 5B). This result provides further support for
 524 explaining Mg/Al ratios < 2 in terms of intimately intermixed low-Mg high-Al phases with Mg-Al
 525 LDH phases, e.g. TAH or N-A-S(-H) gel, because the low Mg/Al ratio of this solid solution phase is 2

526 (Richardson, 2013). However, the simulations predict that the fraction of Al in C-(N)-A-S-H gel
527 (Al_{CNASH}) relative to the total amount of Al in the reaction products ($\text{Al}_{\text{CNASH}}/\text{Al}_{\text{products}}$) is ~0.28 for
528 slag reaction extents >50% (Figure 5A), which is much less than the relative amount of four-
529 coordinated Al ($\text{Al}[4]$) assigned to the reaction products ($\text{Al}[4]/\text{Al}_{\text{products}}$) in ^{27}Al MAS NMR spectral
530 deconvolution analysis of this NS-AS cement ($\text{Al}[4]/\text{Al}_{\text{products}} = 0.60\text{-}0.75$) (Myers et al., 2015a).
531 These ratios, $\text{Al}_{\text{CNASH}}/\text{Al}_{\text{products}}$ and $\text{Al}[4]/\text{Al}_{\text{products}}$, would be comparable if C-(N)-A-S-H gel were the
532 only major Al[4]-bearing solid phase present in AAS cements (i.e. $\text{Al}_{\text{CNASH}}/\text{Al}[4] \approx 1$), but that is not
533 the case here. Recent solubility results for C-(N)-A-S-H gel (Myers et al., 2015b) do not support any
534 further increase in the stability of the Al-containing end-members in the CNASH_ss thermodynamic
535 model, meaning that this discrepancy in the distribution of Al[4] is probably due to other factors.
536 These factors may include incomplete description of other Al[4]-containing phases in the
537 thermodynamic database used here, or that the discrepancy is founded in the experimental ^{29}Si and
538 ^{27}Al MAS NMR analysis. Both options are now discussed.

539
540 The amount of strätlingite predicted by the thermodynamic modelling (Figures 2-5) was likely
541 overestimated because this phase is not clearly distinguished in X-ray diffractograms of sodium
542 silicate-activated slag cements cured for up to 3 years (Ben Haha et al., 2012; Burciaga-Díaz and
543 Escalante-García, 2013; Wang and Scrivener, 1995), or in NS-AS/4 mass% PC blends cured for 3
544 years (Bernal et al., 2012). The solubility product used to describe this phase (Table 1) has an
545 estimated uncertainty interval of ± 1 log unit derived directly from the scatter in the available
546 solubility data for this phase (see Matschei et al. (2007) and references therein), and so an error in this
547 value is unlikely to contribute significantly to the over-prediction of this phase. Therefore, it is likely
548 that additional solid phase(s) are missing from the thermodynamic database used here (Table 1),
549 which would be predicted to form in preference to strätlingite if they were present in the simulation.
550 These may be zeolites such as gismondine and thomsonite (Bernal et al., 2011; Bernal et al., 2014b),
551 or poorly ordered Q⁴-type N-A-S(-H) ('geopolymer') gels (Myers et al., 2013), each of which will
552 accommodate Al in tetrahedral form and could account for the difference between the high tetrahedral
553 fraction determined experimentally, and the notably lower tetrahedral fraction predicted in the current

554 simulations. Thermodynamic data are available for a large number of zeolites (see the compilation by
555 Arthur et al. (2011) for example), but the large variety of possible chemical compositions and the
556 availability of only a few data for each zeolite framework type (often only one datum), mean that
557 more thermochemical or solubility data are needed to better define these phases in thermodynamic
558 databases.

559

560 The maximum possible amount of Al[4] attributable to zeolites or N-A-S(-H) gel is, however, limited
561 by the intensity of the ^{27}Al MAS NMR spectra of this NS-AS cement (Myers et al., 2015a) at ~60
562 ppm (relative to $\text{Al}(\text{H}_2\text{O})_6^{3+}$), which is the typical observed chemical shift at which Al[4] resonates in
563 these phases (Davidovits, 1991; Duxson et al., 2007; Fyfe et al., 1982). Consequently, it is unlikely
564 that zeolites and N-A-S(-H) gel can account for the large discrepancy between the modelled amount
565 of Al[4] in C-(N)-A-S-H gel ($\text{Al}_{\text{CNASH}}/\text{Al}_{\text{products}} \approx 0.28$, Figure 5A) and the experimentally observed
566 amount of Al[4] assigned to reaction products ($\text{Al}[4]/\text{Al}_{\text{products}} = 0.60-0.75$ (Myers et al., 2015a)).
567 Further explanation for this discrepancy can be found in the assumption of congruent slag dissolution
568 applied in the analysis of ^{29}Si and ^{27}Al MAS NMR spectra used as experimental data here (Bernal et
569 al., 2014b; Myers et al., 2015a), which may not be fully attained in slag-based cements, and could
570 significantly alter the deconvolution analysis presented due to the different lineshapes of partially
571 reacted and unreacted slag (Dyson et al., 2007). Development of this understanding will be essential
572 to further enhance the accuracy of the characterisation and simulation of the complex phase
573 assemblages which are formed in AAS-based cements.

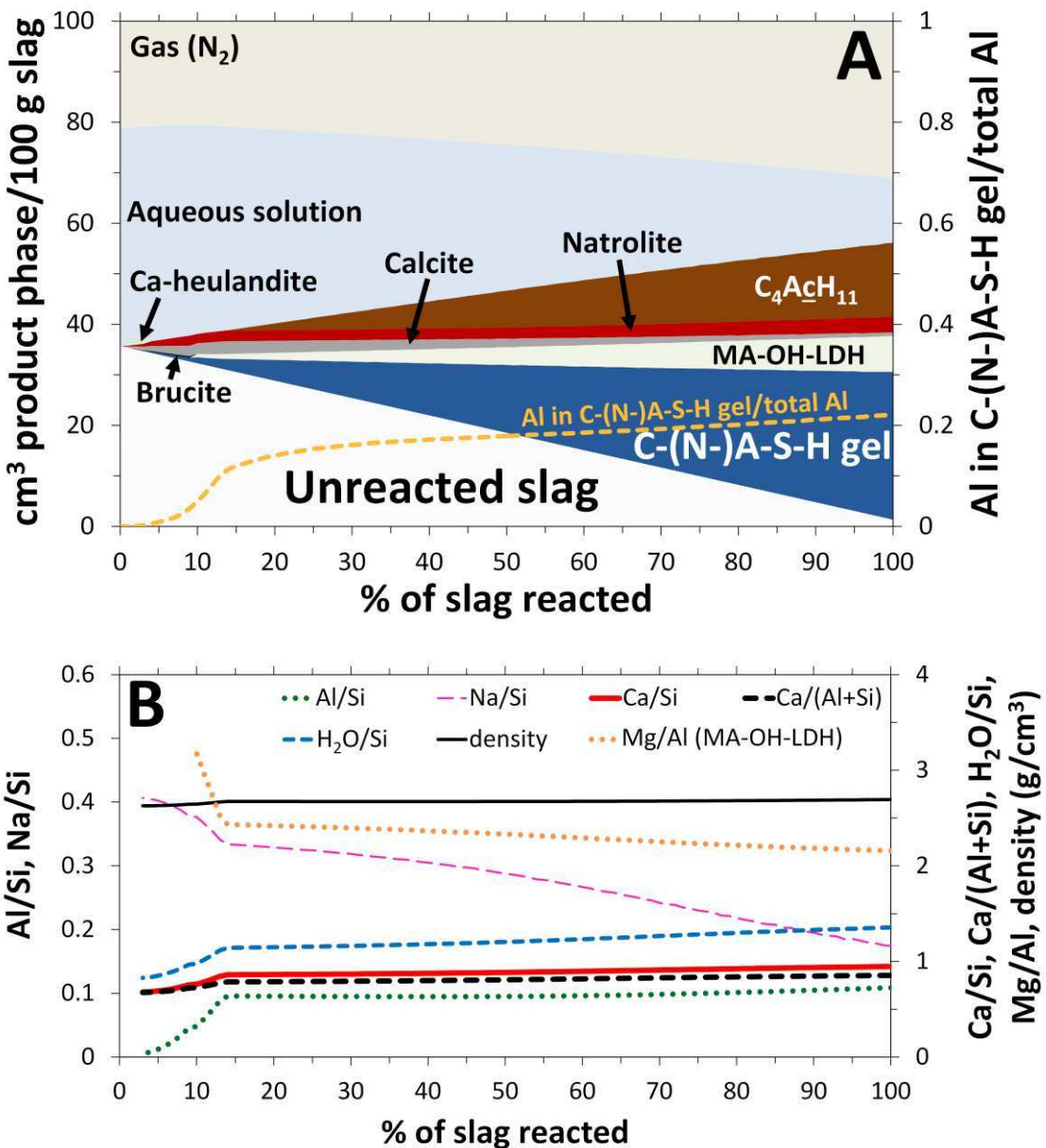
574

575 **3.3 Simulated reaction of a Na_2CO_3 -activated slag cement**

576 The reaction of a Nc -AS cement is simulated via the same procedure used in the simulation of NS-AS
577 cement discussed in section 3.2, except for the change in activator. The simulated solid phase
578 assemblage contains C-(N)-A-S-H gel as the primary reaction product (Figure 7A). The additional
579 products are $\text{C}_4\text{AcH}_{11}$, MA-OH-LDH, calcite and natrolite. The prediction of calcite is consistent with
580 the observation of CaCO_3 polymorphs in Nc -AS cements cured for 20 months (Sakulich et al., 2010)

581 and 180 days (Bernal et al., 2015). Simulation of natrolite and Ca-heulandite is also in good
582 agreement with the identification of heulandite and zeolite-A in Nc-AS cement (Bernal et al., 2015).
583 The modelling results presented here and in section 3.3 are consistent with the identification of more
584 prominent peaks for zeolites in X-ray diffraction patterns for Nc-activated (Bernal et al., 2015),
585 compared to NS-activated, slag cements (Bernal et al., 2014b). C₄A₂H₁₁ has been identified in X-ray
586 diffractograms of Nc-AS pastes cured for 1 day and for 540 days (Shi et al., 2006), although this
587 phase is not always observable (Bernal et al., 2015; Sakulich et al., 2010) due to its tendency to be
588 present as intermixed (Richardson et al., 1994) and/or poorly crystalline structures (Wang and
589 Scrivener, 1995). The simulated chemical shrinkage extents for Nc-AS (Figure 7) and NS-AS cements
590 (Figure 5) at 100% slag reaction extent are comparable, at 11 cm³/100 g slag.

591



592
593 Figure 7. Simulated A) solid phase assemblages and B) C-(N-)A-S-H gel chemical compositions and
594 densities (g/cm^3), and Mg/Al ratios in MA-OH-LDH in an Nc-AS cement using the slag chemical
595 composition in Table 4.
596
597

598 Mg-Al LDH phases are experimentally observed in Nc-AS cements after 180 days (Bernal et al.,
599 2015) and 55 days (Sakulich et al., 2009) of curing, in good agreement with the predicted phase
600 assemblage (Figure 7A). Here, MA-c-LDH is not predicted despite the high availability of CO_2 ,
601 demonstrating the very high stability of MA-OH-LDH under the $\text{pH} \geq 13$ conditions in a hardened
602 Nc-AS cement. Further clarification of this result is needed because recent ^{27}Al MAS NMR results for
603 superficially carbonated NS-AS cements (Myers et al., 2015a), and carbonation depth analysis of

604 these materials after exposure to air for 16 months (Bernal et al., 2014b) can be interpreted in support
605 of the formation of Mg-Al LDH phases intercalated with CO_3^{2-} . Detailed assessment of solubility and
606 thermochemical data for Mg-Al LDH phases intercalated with OH^- and CO_3^{2-} (Bennett et al., 1992;
607 Gao and Li, 2012; Johnson and Glasser, 2003; Morimoto et al., 2012; Rozov et al., 2011) indicates
608 that the solubility product used to describe the $\text{Mg}/\text{Al} = 2$ MA-OH-LDH end-member of the MA-OH-
609 LDH_ss thermodynamic model here may be in error by as much as several log units (Figure 1) and
610 demonstrates the need for further studies of the thermodynamic properties of Mg-Al LDH phases.

611

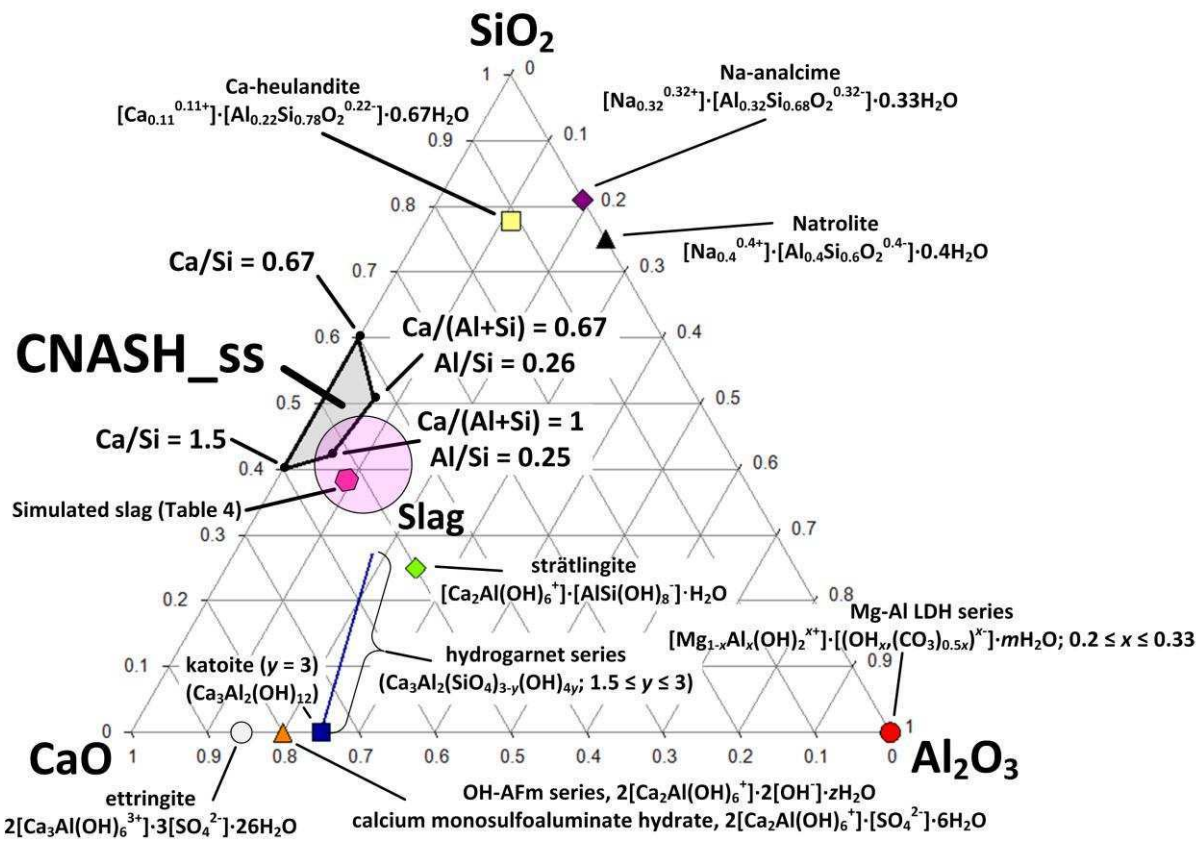
612 Gaylussite has been observed in Nc-AS cement at early age (Bernal et al., 2015) but is not present in
613 the solid phase assemblage simulated here (Figure 7); this phase is slightly undersaturated at low slag
614 reaction extents at $\sim 25^\circ\text{C}$ (Bury and Redd, 1933; Königsberger et al., 1999). This difference indicates
615 that kinetic factors enable the formation of gaylussite in Nc-AS cement cured at room temperature,
616 and this is consistent with its observed consumption as the reaction proceeds (Bernal et al., 2015).

617

618 **3.4 Phase diagrams for alkali-activated slag-based cements**

619 The prediction of several reaction products in the simulated AAS cements is consistent with the bulk
620 chemical composition of the mixes, which generally lie outside the composition envelope of phase-
621 pure C-(N-)A-S-H gel (Figure 8).

622



623
624 Figure 8. Projection of the chemical composition of some reaction products in AAS-based cements
625 onto the $\text{CaO}-\text{SiO}_2-\text{Al}_2\text{O}_3$ ternary system. The grey and pink shaded regions are the composition range
626 described by the CNASH_ss thermodynamic model for C-(N)-A-S-H gel (Myers et al., 2014), and the
627 typical bulk chemical composition range of slag, respectively. The simulated slag described in Table 4
628 is represented by the pink hexagon.
629

630 Further analysis of AAS cement chemistry is performed by simulating phase diagrams at a fixed slag
631 reaction extent of 60%, a constant amount of H_2S (equivalent in S content to a slag composition of 2
632 mass% SO_3 , which is taken as a representative value of S content in slags studied in the literature
633 (Ben Haha et al., 2011a; Bernal et al., 2014b; Gruskovnjak et al., 2006; Puertas et al., 2011;
634 Richardson et al., 1994; Shi et al., 2006)) and slag compositions of either 30 or 40 mass% SiO_2 , with
635 the remaining chemical composition specified in terms of CaO , Al_2O_3 and MgO only. The CaO -
636 Al_2O_3 - MgO composition range selected here was chosen to represent the bulk chemical composition
637 range relevant to AAS-based cements.

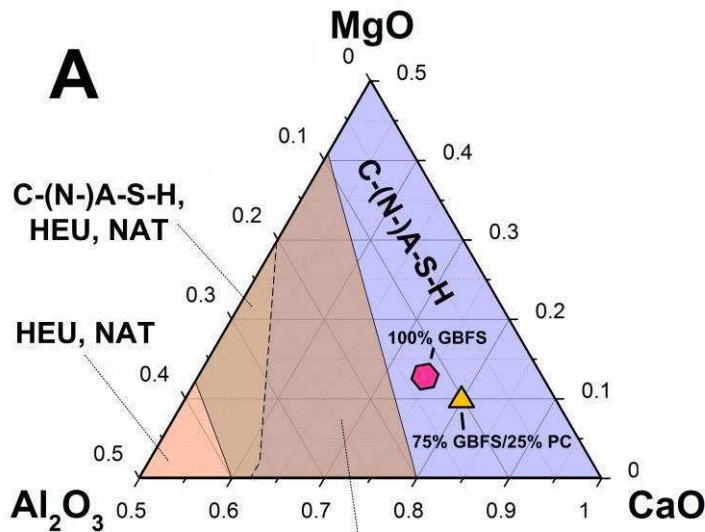
638
639 Zeolites are predicted in every phase diagram for the AAS cements simulated (shown for NS-AS
640 cements only in Figure 9), and are more prominent at higher Si (i.e. lower Ca) and Al concentrations,
641 but only Ca-heulandite and natrolite are predicted among the zeolites included in the thermodynamic

642 database (Table 1). The CaO-Al₂O₃-MgO composition region where C-(N-)A-S-H gel and zeolites are
643 both simulated indicates where C-(N-)A-S-H and N-A-S(-H) gels are likely to coexist in AAS
644 cements, due to the fundamental similarities of zeolites and N-A-S(-H) ('geopolymer') gels (Provis et
645 al., 2005). Inclusion of reliable thermodynamic data for N-A-S(-H) gel and zeolites will be necessary
646 to clarify the chemical compositional envelope in which these gels can coexist. The prediction of
647 zeolites here, in both the higher pH ((NH)_{0.5}-AS) and lower pH systems (N_c-AS), Figures 7 and 9,
648 indicates that increasing pH does not destabilise these phases and the corresponding N-A-S(-H) gel in
649 favour of C-(N-)A-S-H gel in the pH and chemical composition range relevant to cements, as was
650 proposed previously by García-Lodeiro et al. (2011). The increased stability of zeolites at lower CaO
651 content (Figure 4), or alternatively higher Si and Al concentrations (Figure 9) – i.e. decreasing
652 CaO/(Al₂O₃ + SiO₂) – demonstrates that control of Ca-Al-Si compositions is needed to form alkali-
653 activated cements with mixed C-(N-)A-S-H and N-A-S(-H) gels (Ismail et al., 2014). Figure 9 shows
654 that mixtures of C-(N-)A-S-H gel and zeolites are expected to be stable in Na₂SiO₃-activated 75
655 mass% GBFS/25 mass% fly ash (FA) (overall precursor SiO₂ content = 41 mass% based on the FA
656 chemical composition from (Bernal et al., 2013)) or metakaolin (MK) cements (overall precursor SiO₂
657 content = 38 mass% based on the MK chemical composition from (Bernal et al., 2011)), but not in a
658 hybrid system of Na₂SiO₃-activated 75 mass% GBFS/25 mass% PC (based on a PC chemical
659 composition of 19.7 mass% SiO₂, 63.2 mass% CaO, 1.85 mass% MgO, 4.7 mass% Al₂O₃, 3.35
660 mass% SO₃ (Lothenbach and Winnefeld, 2006)). Figure 9 also shows that the stability of zeolites, and
661 therefore of N-A-S(-H) gels, in NS-AS cement depends greatly on the slag SiO₂ content.

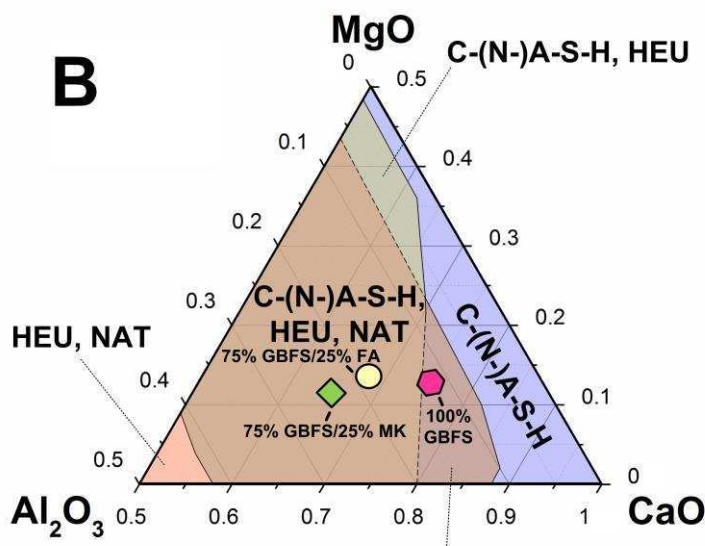
662

663

664



665



666

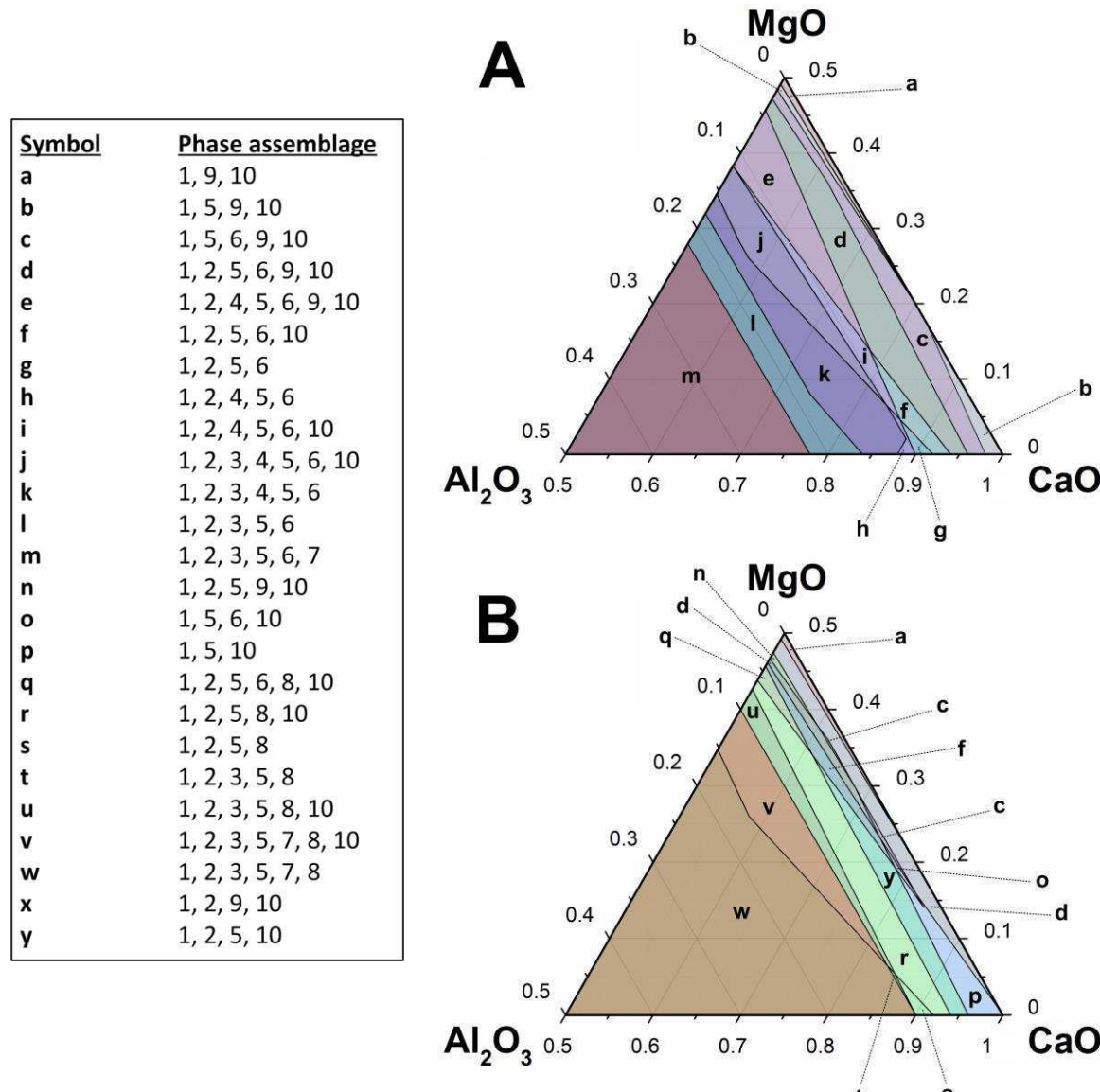
667 Figure 9. Phase diagrams for NS-AS-based cement systems with overall precursor chemical
 668 compositions of 2 mass% SO_3 equivalent and A) 30 mass% SiO_2 and B) 40 mass% SiO_2 , with only
 669 the regions of stability for C-(N)-A-S-H gel and zeolites shown (Mg-containing phases are also
 670 typical reaction products: MA-OH-LDH at moderate and high Al_2O_3 content
 671 ($\text{Al}_2\text{O}_3/(\text{CaO}+\text{Al}_2\text{O}_3+\text{MgO}) > 0.1$); and brucite at moderate and low Al_2O_3 concentrations
 672 ($\text{Al}_2\text{O}_3/(\text{CaO}+\text{Al}_2\text{O}_3+\text{MgO}) < 0.25$)). See text for the GBFS, FA, MK and PC chemical compositions
 673 used. The w/b ratio is 0.4, the overall precursor reaction extent is 60% and the units are in mole
 674 fraction.

675

676 Simulated phase diagrams for $(\text{NH})_{0.5}$ -AS-based cements are shown in Figure 10. The dominant solids
 677 in the simulated phase diagrams for $(\text{NH})_{0.5}$ -AS-based cements (Figure 10) are C-(N)-A-S-H gel and
 678 MA-OH-LDH. C-(N)-A-S-H gel is simulated over the full range of modelled $\text{CaO}-\text{Al}_2\text{O}_3-\text{MgO}$
 679 compositions, and MA-OH-LDH is predicted everywhere in this composition range except at very
 680 low Al_2O_3 content ($\text{Al}_2\text{O}_3/(\text{CaO}+\text{Al}_2\text{O}_3+\text{MgO}) < 0.05$).

681

682



684

685 Figure 10. Phase diagrams in the relevant bulk CaO-Al₂O₃-MgO composition range for (NH)_{0.5}-AS-
686 based cements with A) 30 and B) 40 mass% slag SiO₂ content, and 2 mass% SO₃ equivalent. The
687 phases are: 1, C-(N)-A-S-H gel; 2, MA-OH-LDH; 3, strätlingite; 4, katoite; 5, ettringite; 6, calcium
688 monosulfoaluminate hydrate; 7, natrolite; 8, Ca-heulandite; 9, portlandite; and 10, brucite. The w/b
689 ratio is 0.4, the slag reaction extent is 60% and the units are in mole fraction.
690

691 Ettringite is predicted over a much larger range of CaO-Al₂O₃-MgO compositions than calcium
692 monosulfoaluminate hydrate. These phases are predicted to form here for slag with 2 mass% SO₃
693 equivalent but not for slag containing 0.8 mass% equivalent SO₃ (Table 4). Katoite is only present in
694 the phase diagrams for slags with 30 mass% SiO₂ in the (NH)_{0.5}-AS system. Portlandite is more
695 prominent in the 30 mass% SiO₂ (NH)_{0.5}-AS system (Figure 10A), but is only formed at relatively low

696 Al₂O₃ content (Al₂O₃/(CaO+Al₂O₃+MgO) ≤ 0.12). Brucite is predicted in both phase diagrams, but
697 not at high Al₂O₃ concentrations (Al₂O₃/(CaO+Al₂O₃+MgO) > 0.2). Natrolite and Ca-heulandite are
698 the only zeolites simulated in the phase diagrams. Ca-heulandite has a larger stability region than
699 natrolite in the 40 mass% SiO₂ system, but is not predicted at a SiO₂ content of 30 mass%, where only
700 natrolite is simulated. However, the overall CaO-Al₂O₃-MgO composition region where zeolites are
701 stable in (NH)_{0.5}-AS-based cements increases as a function of increasing slag SiO₂ content, which is
702 consistent with the trends in zeolite stability described above for NS-AS-based cements (Figures 4
703 and 9). Similarly, the CaO-Al₂O₃-MgO composition range where strätlingite is stable is larger in the
704 40 mass% SiO₂ (NH)_{0.5}-AS cement system. These phases, strätlingite, natrolite and Ca-heulandite are
705 only simulated for Al₂O₃/(CaO+Al₂O₃+MgO) ratios > 0.1, showing that intermediate to high Al
706 concentrations are needed to stabilise these phases in (NH)_{0.5}-AS-based cements.

707

708 The phase diagrams presented here provide a framework for predicting solid phase assemblages in
709 AAS cements, which can be improved with more relevant data, e.g. development of the
710 thermodynamic database used (Tables 1-3). This work improves the way in which high-performance
711 AAS-based cements can be designed, by linking the volumetric properties and solid phases formed in
712 these cements to the raw materials used in their production. This framework also represents an
713 important step towards predicting the durability of AAS-based cements, although further work is
714 needed to link the key degradation mechanisms, e.g. carbonation, with the volumetric properties
715 (Provis et al., 2012) and phase assemblages (Bernal et al., 2014b) in these cements.

716

717

718 **4. Conclusions**

719

720 This paper has presented a thermodynamic modelling analysis of AAS-based cements. The
721 thermodynamic database used contains a CNASH_ss thermodynamic model for C-(N-)A-S-H gel,
722 which explicitly describes Na and tetrahedral Al incorporated into this phase, a MA-OH-LDH_ss

723 ideal solid solution thermodynamic model for MA-OH-LDH, and thermodynamic data for some alkali
724 carbonate and zeolite phases. The thermodynamic database presented here extends the utility of
725 thermodynamic modelling in predicting the long-term chemistry of AAS-based cements, which is
726 important for application of these materials, e.g. in the design of high performance cements for
727 construction and in nuclear waste disposal applications, and further promotes the valorisation of
728 metallurgical slags.

729

730 Thermodynamic modelling of NS-AS cements generally showed that the CNASH_ss thermodynamic
731 model described the Al/Si ratios of the C-(N-)A-S-H gels formed in the most relevant composition
732 range/alkali content for the majority of AAS cements. The Mg/Al ratios of the simulated MA-OH-
733 LDH phase was generally in good agreement with experimental results for this phase in AAS
734 cements, although additional thermodynamic data for MA-OH-LDH are needed to clarify the stability
735 of this phase in carbonated and Nc-activated cement. Additional thermodynamic data for other
736 reaction products such as TAH, zeolites and N-A-S(-H) gels are also needed for better consistency
737 with the experimental Al/Si ratios in C-(N-)A-S-H gel and Mg/Al ratios in Mg-Al LDH. Simulated
738 solid phase assemblages for NS-AS cements compared closely to the solid phases identified
739 experimentally in these materials, and the simulations accurately predicted the experimentally
740 measured chemical shrinkage in a NS-AS cement.

741

742 Phase diagrams for $(\text{NH})_{0.5}\text{-AS}$ - and NS-AS-based cements were simulated, which showed that C-(N-)
743)A-S-H gel and MA-OH-LDH are formed over the majority of chemical compositions relevant to
744 these cements. Natrolite and Ca-heulandite featured more prominently in the phase diagrams at lower
745 CaO concentration, and higher SiO_2 and Al_2O_3 content, indicating that the bulk $\text{CaO}/(\text{SiO}_2 + \text{Al}_2\text{O}_3)$
746 ratio plays a significant role in stabilising zeolites, and therefore N-A-S(-H) gels, in AAS-based
747 cements. Zeolites were predicted to be stable in NS-activated 75 mass% GBFS/25 mass% FA and MK
748 cements but not in hybrid NS-activated 75 mass% GBFS/25 mass% PC. Therefore, these phase
749 diagrams can be used as a reference tool for the development of high-performance AAS-based

750 cements, by enabling solid phase assemblages for these cements to be predicted from the bulk
751 compositions of the raw materials used.

752

753 **5. Acknowledgements**

754 The authors thank the Faculty of Engineering, University of Sheffield, for funding, and an anonymous
755 reviewer who helped to improve the quality of the manuscript.

756

757 **6. References**

758 Allada, R., Navrotsky, A. and Boerio-Goates, J. (2005) Thermochemistry of hydrotalcite-like phases
759 in the MgO-Al₂O₃-CO₂-H₂O system: a determination of enthalpy, entropy, and free energy. Am.
760 Mineral. **90**, 329-335.

761 Andersen, M.D., Jakobsen, H.J. and Skibsted, J. (2006) A new aluminium-hydrate species in hydrated
762 Portland cements characterized by ²⁷Al and ²⁹Si MAS NMR spectroscopy. Cem. Concr. Res. **36**, 3-17.

763 Anderson, G.M. and Crerar, D.A. (1993) Thermodynamics in geochemistry: the equilibrium model.
764 Oxford University Press, Oxford.

765 Arthur, R., Sasamoto, H., Walker, C. and Yui, M. (2011) Polymer model of zeolite thermochemical
766 stability. Clays Clay Miner. **59**, 626-639.

767 Atkins, M., Bennett, D.G., Dawes, A.C., Glasser, F.P., Kindness, A. and Read, D. (1992) A
768 thermodynamic model for blended cements. Cem. Concr. Res. **22**, 497-502.

769 Babushkin, I., Matveev, G.M. and Mchedlow-Petrosyan, O.P. (1985) Thermodynamics of silicates.
770 Springer-Verlag, Berlin.

771 Baerlocher, C., McCusker, L.B. and Olson, D.H. (2007) Atlas of zeolite framework types. Elsevier,
772 Netherlands.

773 Bai, Y., Collier, N.C., Milestone, N.B. and Yang, C.H. (2011) The potential for using slags activated
774 with near neutral salts as immobilisation matrices for nuclear wastes containing reactive metals. J.
775 Nucl. Mater. **413**, 183-192.

- 776 Ben Haha, M., Le Saoût, G., Winnefeld, F. and Lothenbach, B. (2011a) Influence of activator type on
777 hydration kinetics, hydrate assemblage and microstructural development of alkali activated blast-
778 furnace slags. *Cem. Concr. Res.* **41**, 301-310.
- 779 Ben Haha, M., Lothenbach, B., Le Saoût, G. and Winnefeld, F. (2011b) Influence of slag chemistry
780 on the hydration of alkali-activated blast-furnace slag - part I: effect of MgO. *Cem. Concr. Res.* **41**,
781 955-963.
- 782 Ben Haha, M., Lothenbach, B., Le Saoût, G. and Winnefeld, F. (2012) Influence of slag chemistry on
783 the hydration of alkali-activated blast-furnace slag - part II: effect of Al₂O₃. *Cem. Concr. Res.* **42**, 74-
784 83.
- 785 Bennett, D.G., Read, D., Atkins, M. and Glasser, F.P. (1992) A thermodynamic model for blended
786 cements. II: cement hydrate phases; thermodynamic values and modelling studies. *J. Nucl. Mater.*
787 **190**, 315-325.
- 788 Bernal, S.A., Provis, J.L., Rose, V. and Mejía De Gutierrez, R. (2011) Evolution of binder structure in
789 sodium silicate-activated slag-metakaolin blends. *Cem. Concr. Compos.* **33**, 46-54.
- 790 Bernal, S.A., Provis, J.L., Brice, D.G., Kilcullen, A., Duxson, P. and van Deventer, J.S.J. (2012)
791 Accelerated carbonation testing of alkali-activated binders significantly underestimates service life:
792 the role of pore solution chemistry. *Cem. Concr. Res.* **42**, 1317-1326.
- 793 Bernal, S.A., Provis, J.L., Walkley, B., San Nicolas, R., Gehman, J.G., Brice, D.G., Kilcullen, A.,
794 Duxson, P. and van Deventer, J.S.J. (2013) Gel nanostructure in alkali-activated binders based on slag
795 and fly ash, and effects of accelerated carbonation. *Cem. Concr. Res.* **53**, 127-144.
- 796 Bernal, S.A., Rose, V. and Provis, J.L. (2014a) The fate of iron in blast furnace slag particles during
797 alkali-activation. *Mater. Chem. Phys.* **146**, 1-5.
- 798 Bernal, S.A., San Nicolas, R., Myers, R.J., Mejía de Gutiérrez, R., Puertas, F., van Deventer, J.S.J.
799 and Provis, J.L. (2014b) MgO content of slag controls phase evolution and structural changes induced
800 by accelerated carbonation in alkali-activated binders. *Cem. Concr. Res.* **57**, 33-43.
- 801 Bernal, S.A., Provis, J.L., Myers, R.J., San Nicolas, R. and van Deventer, J.S.J. (2015) Role of
802 carbonates in the chemical evolution of sodium carbonate-activated slag binders. *Mater. Struct.* **48**,
803 517-529.

- 804 Bonk, F., Schneider, J., Cincotto, M.A. and Panepucci, H. (2003) Characterization by multinuclear
805 high-resolution NMR of hydration products in activated blast-furnace slag pastes. *J. Am. Ceram. Soc.*
806 **86**, 1712-1719.
- 807 Brough, A.R. and Atkinson, A. (2002) Sodium silicate-based, alkali-activated slag mortars - part I.
808 Strength, hydration and microstructure. *Cem. Concr. Res.* **32**, 865-879.
- 809 Burciaga-Díaz, O. and Escalante-García, J.I. (2013) Structure, mechanisms of reaction, and strength
810 of an alkali-activated blast-furnace slag. *J. Am. Ceram. Soc.* **96**, 3939-3948.
- 811 Bury, C.R. and Redd, R. (1933) The system sodium carbonate-calcium carbonate-water. *J. Chem.*
812 *Soc.*, 1160-1162.
- 813 Chen, W. and Brouwers, H.J.H. (2007) The hydration of slag, part 1: reaction models for alkali-
814 activated slag. *J. Mater. Sci.* **42**, 428-443.
- 815 Davidovits, J. (1991) Geopolymers - inorganic polymeric new materials. *J. Therm. Anal.* **37**, 1633-
816 1656.
- 817 de Wolff, P.M. (1952) The crystal structure of artinite, $Mg_2(OH)_2CO_3 \cdot 3H_2O$. *Acta Crystallogr.* **5**,
818 286-287.
- 819 Dickens, B. and Brown, W.E. (1969) Crystal structures of $CaNa_2(CO_3)_2 \cdot 5H_2O$, synthetic gaylussite,
820 and $CaNa_2(CO_3)_2 \cdot 2H_2O$, synthetic pirssonite. *Inorg. Chem.* **8**, 2093-2103.
- 821 Dilnesa, B.Z., Lothenbach, B., Renaudin, G., Wichser, A. and Kulik, D. (2014) Synthesis and
822 characterization of hydrogarnet $Ca_3(Al_xFe_{1-x})_2(SiO_4)_y(OH)_{4(3-y)}$. *Cem. Concr. Res.* **59**, 96-111.
- 823 Duxson, P., Fernandez-Jimenez, A., Provis, J.L., Lukey, G.C., Palomo, A. and van Deventer, J.S.J.
824 (2007) Geopolymer technology: the current state of the art. *J. Mater. Sci.* **42**, 2917-2933.
- 825 Dyson, H.M., Richardson, I.G. and Brough, A.R. (2007) A combined ^{29}Si MAS NMR and selective
826 dissolution technique for the quantitative evaluation of hydrated blast furnace slag cement blends. *J.*
827 *Am. Ceram. Soc.* **90**, 598-602.
- 828 Fyfe, C.A., Gobbi, G.C., Hartman, J.S., Klinowski, J. and Thomas, J.M. (1982) Solid-state magic-
829 angle spinning. Aluminum-27 nuclear magnetic resonance studies of zeolites using a 400-MHz high-
830 resolution spectrometer. *J. Phys. Chem.* **86**, 1247-1250.
- 831 Gao, W. and Li, Z. (2012) Solubility and K_{SP} of $Mg_4Al_2(OH)_{14} \cdot 3H_2O$ at the various ionic strengths.
832 *Hydrometallurgy* **117-118**, 36-46.

- 833 García-Lodeiro, I., Palomo, A., Fernández-Jiménez, A. and MacPhee, D.E. (2011) Compatibility
834 studies between N-A-S-H and C-A-S-H gels. Study in the ternary diagram Na₂O-CaO-Al₂O₃-SiO₂-
835 H₂O. *Cem. Concr. Res.* **41**, 923-931.
- 836 Glasser, F.P. and Atkins, M. (1994) Cements in radioactive waste disposal. *MRS Bull.* **19**, 33-38.
- 837 Graf, D.L. and Bradley, W.F. (1962) The crystal structure of huntite, Mg₃Ca(CO₃)₄. *Acta Crystallogr.*
838 **15**, 238-242.
- 839 Gruskovnjak, A., Lothenbach, B., Holzer, L., Figi, R. and Winnefeld, F. (2006) Hydration of alkali-
840 activated slag: comparison with ordinary Portland cement. *Adv. Cem. Res.* **18**, 119-128.
- 841 Helgeson, H.C., Delany, J.M. and Nesbitt, H.W. (1978) Summary and critique of the thermodynamic
842 properties of rock-forming minerals. *Am. J. Sci.* **278-A**, 1-229.
- 843 Helgeson, H.C., Kirkham, D.H. and Flowers, G.C. (1981) Theoretical prediction of the
844 thermodynamic behavior of aqueous electrolytes at high pressures and temperatures: IV. Calculation
845 of activity coefficients, osmotic coefficients, and apparent molal and standard and relative partial
846 molal properties to 600°C and 5 kb. *Am. J. Sci.* **281**, 1249-1516.
- 847 Hemingway, B.S. and Robie, R.A. (1972) The heat capacities at low temperatures and entropies at
848 298.15K of huntite, CaMg₃(CO₃)₄, and artinite, Mg₂(OH)₂CO₃·3H₂O. *Am. Mineral.* **57**, 1754-1767.
- 849 Hill, R.J., Canterford, J.H. and Moyle, F.J. (1982) New data for lansfordite. *Mineral. Mag.* **46**, 453-
850 457.
- 851 Hummel, W., Berner, U., Curti, E., Pearson, F.J. and Thoenen, T. (2002) Nagra/PSI Chemical
852 Thermodynamic Database 01/01. Universal Publishers, Parkland, Florida.
- 853 Ismail, I., Bernal, S.A., Provis, J.L., San Nicolas, R., Hamdan, S. and van Deventer, J.S.J. (2014)
854 Modification of phase evolution in alkali-activated blast furnace slag by the incorporation of fly ash.
855 *Cem. Concr. Compos.* **45**, 125-135.
- 856 Jennings, H.M. (2008) Refinements to colloid model of C-S-H in cement: CM-II. *Cem. Concr. Res.*
857 **38**, 275-289.
- 858 Jensen, O.M. and Hansen, P.F. (2001) Water-entrained cement-based materials - I. Principles and
859 theoretical background. *Cem. Concr. Res.* **31**, 647-654.

- 860 Johnson, C.A. and Glasser, F.P. (2003) Hydrotalcite-like minerals ($M_2Al(OH)_6(CO_3)_{0.5}\cdot XH_2O$, where
861 M = Mg, Zn, Co, Ni) in the environment: synthesis, characterization and thermodynamic stability.
862 *Clays Clay Miner.* **51**, 1-8.
- 863 Johnson, G.K., Flotow, H.E. and O'Hare, P.A.G. (1982) Thermodynamic studies of zeolites; analcime
864 and dehydrated analcime. *Am. Mineral.* **67**, 736-748.
- 865 Johnson, G.K., Flotow, H.E., O'Hare, P.A.G. and Wise, W.S. (1983) Thermodynamic studies of
866 zeolites; natrolite, mesolite and scolecite. *Am. Mineral.* **68**, 1134-1145.
- 867 Johnson, J.W., Oelkers, E.H. and Helgeson, H.C. (1992) SUPCRT92: A software package for
868 calculating the standard molal thermodynamic properties of minerals, gases, aqueous species, and
869 reactions from 1 to 5000 bar and 0 to 1000°C. *Comput. Geosci.* **18**, 899-947.
- 870 Kiseleva, I., Navrotsky, A., Belitsky, I. and Furseko, B. (2001) Thermochemical study of calcium
871 zeolites—heulandite and stilbite. *Am. Mineral.* **86**, 448-455.
- 872 Königsberger, E., Königsberger, L.-C. and Gamsjäger, H. (1999) Low-temperature thermodynamic
873 model for the system $Na_2CO_3-MgCO_3-CaCO_3-H_2O$. *Geochim. Cosmochim. Acta* **63**, 3105-3119.
- 874 Kulik, D.A. and Kersten, M. (2001) Aqueous solubility diagrams for cementitious waste stabilization
875 systems: II. End-member stoichiometries of ideal calcium silicate hydrate solid solutions. *J. Am.*
876 *Ceram. Soc.* **84**, 3017-3026.
- 877 Kulik, D.A. (2011) Improving the structural consistency of C-S-H solid solution thermodynamic
878 models. *Cem. Concr. Res.* **41**, 477-495.
- 879 Kulik, D.A., Wagner, T., Dmytrieva, S.V., Kosakowski, G., Hingerl, F.F., Chudnenko, K.V. and
880 Berner, U. (2013) GEM-Selektor geochemical modeling package: revised algorithm and GEMS3K
881 numerical kernel for coupled simulation codes. *Comput. Geosci.* **17**, 1-24.
- 882 Le Saoût, G., Ben Haha, M., Winnefeld, F. and Lothenbach, B. (2011) Hydration degree of alkali-
883 activated slags: a ^{29}Si NMR study. *J. Am. Ceram. Soc.* **94**, 4541-4547.
- 884 Lothenbach, B. and Winnefeld, F. (2006) Thermodynamic modelling of the hydration of Portland
885 cement. *Cem. Concr. Res.* **36**, 209-226.
- 886 Lothenbach, B. and Gruskovnjak, A. (2007) Hydration of alkali-activated slag: thermodynamic
887 modelling. *Adv. Cem. Res.* **19**, 81-92.

- 888 Lothenbach, B., Matschei, T., Möschner, G. and Glasser, F.P. (2008) Thermodynamic modelling of
889 the effect of temperature on the hydration and porosity of Portland cement. *Cem. Concr. Res.* **38**, 1-
890 18.
- 891 Lothenbach, B. (2010) Thermodynamic equilibrium calculations in cementitious systems. *Mater.*
892 *Struct.* **43**, 1413-1433.
- 893 Lothenbach, B., Pelletier-Chaignat, L. and Winnefeld, F. (2012) Stability in the system CaO-Al₂O₃-
894 H₂O. *Cem. Concr. Res.* **42**, 1621-1634.
- 895 Matschei, T., Lothenbach, B. and Glasser, F.P. (2007) Thermodynamic properties of Portland cement
896 hydrates in the system CaO-Al₂O₃-SiO₂-CaSO₄-CaCO₃-H₂O. *Cem. Concr. Res.* **37**, 1379-1410.
- 897 McLellan, B.C., Williams, R.P., Lay, J., van Riessen, A. and Corder, G.D. (2011) Costs and carbon
898 emissions for geopolymers pastes in comparison to ordinary portland cement. *J. Cleaner Prod.* **19**,
899 1080-1090.
- 900 Moloy, E.C., Liu, Q. and Navrotsky, A. (2006) Formation and hydration enthalpies of the
901 hydrosodalite family of materials. *Micropor. Mesopor. Mat.* **88**, 283-292.
- 902 Monnin, C. and Schott, J. (1984) Determination of the solubility products of sodium carbonate
903 minerals and an application to trona deposition in Lake Magadi (Kenya). *Geochim. Cosmochim. Acta*
904 **48**, 571-581.
- 905 Morimoto, K., Anraku, S., Hoshino, J., Yoneda, T. and Sato, T. (2012) Surface complexation
906 reactions of inorganic anions on hydrotalcite-like compounds. *J. Colloid Interf. Sci.* **384**, 99-104.
- 907 Möschner, G., Lothenbach, B., Rose, J., Ulrich, A., Figi, R. and Kretzschmar, R. (2008) Solubility of
908 Fe-ettringite (Ca₆[Fe(OH)₆]₂(SO₄)₃·26H₂O). *Geochim. Cosmochim. Acta* **72**, 1-18.
- 909 Möschner, G., Lothenbach, B., Winnefeld, F., Ulrich, A., Figi, R. and Kretzschmar, R. (2009) Solid
910 solution between Al-ettringite and Fe-ettringite (Ca₆[Al_{1-x}Fe_x(OH)₆]₂(SO₄)₃·26H₂O). *Cem. Concr.*
911 *Res.* **39**, 482-489.
- 912 Muller, A.C.A., Scrivener, K.L., Gajewicz, A.M. and McDonald, P.J. (2013) Use of bench-top NMR
913 to measure the density, composition and desorption isotherm of C-S-H in cement paste. *Micropor.*
914 *Mesopor. Mat.* **178**, 99-103.
- 915 Myers, R.J., Bernal, S.A., San Nicolas, R. and Provis, J.L. (2013) Generalized structural description
916 of calcium-sodium aluminosilicate hydrate gels: the cross-linked substituted tobermorite model.
917 *Langmuir* **29**, 5294-5306.

- 918 Myers, R.J., Bernal, S.A. and Provis, J.L. (2014) A thermodynamic model for C-(N)-A-S-H gel:
919 CNASH_{ss}. Derivation and application. *Cem. Concr. Res.* **66**, 27-47.
- 920 Myers, R.J., Bernal, S.A., Provis, J.L., Gehman, J.D. and van Deventer, J.S.J. (2015a) The role of Al
921 in cross-linking of alkali-activated slag cements. *J. Am. Ceram. Soc.* **98**, 996-1004.
- 922 Myers, R.J., L'Hôpital, E., Provis, J.L. and Lothenbach, B. (2015b) Effect of temperature and
923 aluminium on calcium aluminosilicate hydrate chemistry under equilibrium conditions. *Cem. Concr.
924 Res.* **68**, 83-93.
- 925 Provis, J.L., Lukey, G.C. and van Deventer, J.S.J. (2005) Do geopolymers actually contain
926 nanocrystalline zeolites? A reexamination of existing results. *Chem. Mater.* **17**, 3075-3085.
- 927 Provis, J.L., Myers, R.J., White, C.E., Rose, V. and van Deventer, J.S.J. (2012) X-ray
928 microtomography shows pore structure and tortuosity in alkali-activated binders. *Cem. Concr. Res.*
929 **42**, 855-864.
- 930 Provis, J.L. (2014) Geopolymers and other alkali activated materials: why, how, and what? *Mater.
931 Struct.* **47**, 11-25.
- 932 Provis, J.L. and Bernal, S.A. (2014) Geopolymers and related alkali-activated materials. *Annu. Rev.
933 Mater. Res.* **44**, 299-327.
- 934 Puertas, F., Palacios, M., Manzano, H., Dolado, J.S., Rico, A. and Rodríguez, J. (2011) A model for
935 the C-A-S-H gel formed in alkali-activated slag cements. *J. Eur. Ceram. Soc.* **31**, 2043-2056.
- 936 Richardson, I.G. and Groves, G.W. (1993) The incorporation of minor and trace elements into
937 calcium silicate hydrate (C-S-H) gel in hardened cement pastes. *Cem. Concr. Res.* **23**, 131-138.
- 938 Richardson, I.G., Brough, A.R., Groves, G.W. and Dobson, C.M. (1994) The characterization of
939 hardened alkali-activated blast-furnace slag pastes and the nature of the calcium silicate hydrate (C-S-
940 H) phase. *Cem. Concr. Res.* **24**, 813-829.
- 941 Richardson, I.G. (2004) Tobermorite/jennite- and tobermorite/calcium hydroxide-based models for
942 the structure of C-S-H: applicability to hardened pastes of tricalcium silicate, β -dicalcium silicate,
943 Portland cement, and blends of Portland cement with blast-furnace slag, metakaolin, or silica fume.
944 *Cem. Concr. Res.* **34**, 1733-1777.
- 945 Richardson, I.G. (2013) Clarification of possible ordered distributions of trivalent cations in layered
946 double hydroxides and an explanation for the observed variation in the lower solid-solution limit. *Acta
947 Crystallogr. B.* **69**, 629-633.

- 948 Robie, R.A. and Hemingway, B.S. (1995) Thermodynamic properties of minerals and related
949 substances at 298.15 K and 1 bar (10^5 Pascals) pressure and at higher temperatures. United States
950 Government Printing Office, Washington D.C.
- 951 Rozov, K. (2010) Stability and solubility of hydrotalcite-pyroaurite solid solutions: synthesis,
952 characterization and thermodynamic modelling, Department of Science. Ph.D. Thesis, The University
953 of Bern, Bern.
- 954 Rozov, K.B., Berner, U., Kulik, D.A. and Diamond, L.W. (2011) Solubility and thermodynamic
955 properties of carbonate-bearing hydrotalcite-pyroaurite solid solutions with a 3:1 Mg/(Al+Fe) mole
956 ratio. *Clays Clay Miner.* **59**, 215-232.
- 957 Sakulich, A.R., Anderson, E., Schauer, C. and Barsoum, M.W. (2009) Mechanical and
958 microstructural characterization of an alkali-activated slag/limestone fine aggregate concrete. *Constr.*
959 *Build. Mater.* **23**, 2951-2957.
- 960 Sakulich, A.R., Miller, S. and Barsoum, M.W. (2010) Chemical and microstructural characterization
961 of 20-month-old alkali-activated slag cements. *J. Am. Ceram. Soc.* **93**, 1741-1748.
- 962 Savage, D., Soler, J.M., Yamaguchi, K., Walker, C., Honda, A., Inagaki, M., Watson, C., Wilson, J.,
963 Benbow, S., Gaus, I. and Rueedi, J. (2011) A comparative study of the modelling of cement hydration
964 and cement–rock laboratory experiments. *Appl. Geochem.* **26**, 1138-1152.
- 965 Schmidt, T., Lothenbach, B., Romer, M., Scrivener, K., Rentsch, D. and Figi, R. (2008) A
966 thermodynamic and experimental study of the conditions of thaumasite formation. *Cem. Conc. Res.*
967 **38**, 337-349.
- 968 Schneider, J., Cincotto, M.A. and Panepucci, H. (2001) ^{29}Si and ^{27}Al high-resolution NMR
969 characterization of calcium silicate hydrate phases in activated blast-furnace slag pastes. *Cem. Concr.*
970 *Res.* **31**, 993-1001.
- 971 Shi, C., Krivenko, P.V. and Roy, D. (2006) Alkali-Activated Cements and Concretes, 1st ed. Taylor &
972 Francis, New York.
- 973 Shock, E.L., Helgeson, H.C. and Sverjensky, D.A. (1989) Calculation of the thermodynamic and
974 transport properties of aqueous species at high pressures and temperatures: standard partial molal
975 properties of inorganic neutral species. *Geochim. Cosmochim. Acta* **53**, 2157-2183.

- 976 Shock, E.L. and Helgeson, H.C. (1990) Calculation of the thermodynamic and transport properties of
977 aqueous species at high pressures and temperatures: Standard partial molal properties of organic
978 species. *Geochim. Cosmochim. Acta* **54**, 915-945.
- 979 Shock, E.L., Sassani, D.C., Willis, M. and Sverjensky, D.A. (1997) Inorganic species in geologic
980 fluids: correlations among standard molal thermodynamic properties of aqueous ions and hydroxide
981 complexes. *Geochim. Cosmochim. Acta* **61**, 907-950.
- 982 Snellings, R. (2013) Solution-controlled dissolution of supplementary cementitious material glasses at
983 pH 13: the effect of solution composition on glass dissolution rates. *J. Am. Ceram. Soc.* **96**, 2467-
984 2475.
- 985 Sun, G.K., Young, J.F. and Kirkpatrick, R.J. (2006) The role of Al in C-S-H: NMR, XRD, and
986 compositional results for precipitated samples. *Cem. Concr. Res.* **36**, 18-29.
- 987 Sverjensky, D.A., Shock, E.L. and Helgeson, H.C. (1997) Prediction of the thermodynamic properties
988 of aqueous metal complexes to 1000°C and 5 kb. *Geochim. Cosmochim. Acta* **61**, 1359-1412.
- 989 Taga, T. (1969) Crystal structure of $\text{Na}_2\text{CO}_3 \cdot 10\text{H}_2\text{O}$. *Acta Crystallogr. B* **25**, 2656-2658.
- 990 Taylor, R., Richardson, I.G. and Brydson, R.M.D. (2010) Composition and microstructure of 20-year-
991 old ordinary Portland cement-ground granulated blast-furnace slag blends containing 0 to 100% slag.
992 *Cem. Concr. Res.* **40**, 971-983.
- 993 Tazawa, E.-i., Miyazawa, S. and Kasai, T. (1995) Chemical shrinkage and autogenous shrinkage of
994 hydrating cement paste. *Cem. Concr. Res.* **25**, 288-292.
- 995 Thoenen, T. and Kulik, D.A. (2003) Nagra/PSI chemical thermodynamic database 01/01 for the
996 GEM-Selektor (V.2-PSI) geochemical modeling code. Paul Scherrer Institute, Villigen; available at
997 <http://gems.web.psi.ch/TDB/doc/pdf/TM-44-03-04-web.pdf>.
- 998 Thoenen, T., Hummel, W. and Berner, U. (2013) The PSI/Nagra Chemical Thermodynamic Database
999 12/07: present status and future developments. *Mineral. Mag.* **77**, 2327.
- 1000 Thomas, J.J., Allen, A.J. and Jennings, H.M. (2012) Density and water content of nanoscale solid C-
1001 S-H formed in alkali-activated slag (AAS) paste and implications for chemical shrinkage. *Cem.*
1002 *Concr. Res.* **42**, 377-383.
- 1003 van Deventer, J.S.J., Provis, J.L. and Duxson, P. (2012) Technical and commercial progress in the
1004 adoption of geopolymers. *Miner. Eng.* **29**, 89-104.

- 1005 Wagman, D.D., Evans, W.H., Parker, V.B., Schumm, R.H. and Halow, I. (1982) The NBS tables of
1006 chemical thermodynamic properties: selected values for inorganic and C₁ and C₂ organic substances
1007 in SI units. American Chemical Society and the American Institute of Physics for the National Bureau
1008 of Standards, New York.
- 1009 Wagner, T., Kulik, D.A., Hingerl, F.F. and Dmytrieva, S.V. (2012) GEM-Selektor geochemical
1010 modeling package: TSolMod library and data interface for multicomponent phase models. Can.
1011 Mineral. **50**, 1173-1195.
- 1012 Wang, S.D. and Scrivener, K.L. (1995) Hydration products of alkali activated slag cement. Cem.
1013 Concr. Res. **25**, 561-571.
- 1014 Wolery, T.J., Jove-Colon, C.F., Krumhansl, J.L., Spencer, R.E., Brady, P.V. and Freeze, G.A. (2007)
1015 Qualification of thermodynamic data for geochemical modeling of mineral-water interactions in dilute
1016 systems. Sandia National Laboratories, United States, 412 pp.
- 1017
- 1018
- 1019